

1

2 **Investigating size-segregated sources of elemental composition of**  
3 **particulate matter in the South China Sea during the 2011 *Vasco***  
4 **Cruise**

5 **Miguel Ricardo A. Hilario<sup>a, +</sup>, Melliza T. Cruz<sup>b</sup>, Maria Obiminda L. Cambaliza<sup>a,b</sup>, Jeffrey S. Reid<sup>c</sup>,**  
6 **Peng Xian<sup>c</sup>, James B. Simpas<sup>a,b</sup>, Nofel D. Lagrosas<sup>b,\*</sup>, Sherdon Niño Y. Uy<sup>b</sup>, Steve Cliff<sup>d</sup>, Yongjing**  
7 **Zhao<sup>d</sup>**

8 <sup>a</sup> Department of Physics, Ateneo de Manila University, Quezon City, Philippines

9 <sup>b</sup> Manila Observatory, Ateneo de Manila University campus, Quezon City, Philippines

10 <sup>c</sup> Marine Meteorology Division, Naval Research Laboratory, Monterey, CA, USA

11 <sup>d</sup> Air Quality Research Center, University of California Davis, CA, USA

12 <sup>+</sup> Now with Manila Observatory, Ateneo de Manila University campus, Quezon City, Philippines

13 <sup>\*</sup> Now with Center for Environmental Remote Sensing, Chiba University, Japan

14 **Correspondence:** Maria Obiminda L. Cambaliza ([mcambaliza@ateneo.edu](mailto:mcambaliza@ateneo.edu))

15 **Abstract**

16 The South China Sea/West Philippine Sea (SCS/WPS) is a receptor of numerous natural and anthropogenic aerosol  
17 species from throughout greater Asia. A combination of several developing countries, archipelagic/peninsular terrain, a strong  
18 Asian monsoon climate, and a host of multi-scale meteorological phenomena make the SCS/WPS one of the most complex  
19 aerosol-meteorological systems in the world. However, aside from the well-known biomass burning emissions from Indonesia  
20 and Borneo, the current understanding of aerosol sources is limited-especially in remote marine environments. In September  
21 2011, a 2-week research cruise was conducted near Palawan, Philippines to sample the remote SCS/WPS environment. Size-  
22 segregated aerosol data was collected using a Davis Rotating-drum Unit size-cut Monitor sampler and analyzed for  
23 concentrations of 28 elements measured via X-ray fluorescence (XRF). Positive Matrix Factorization (PMF) was performed  
24 separately on the coarse, fine, and ultrafine size ranges to determine possible sources and their contributions to the total  
25 elemental particulate matter mass. The PMF analysis resolved six sources across the three size ranges: biomass burning, oil  
26 combustion, soil dust, a crustal-marine mixed source, sea spray, and fly ash. Additionally, size distribution plots, time series  
27 plots, back trajectories and satellite data were used in interpreting factors. The multi-technique source apportionment revealed

28 the presence of biogenic sources such as soil dust, sea spray and a crustal-marine mixed source; anthropogenic sources were  
29 identified as well: biomass burning, oil combustion, and fly ash. Mass size distributions showed elevated aerosol  
30 concentrations towards the end of the sampling period which coincided with a shift of air mass back trajectories to Southern  
31 Kalimantan. Covariance between coarse mode soil dust and fine mode biomass burning aerosols were observed. Agreement  
32 between the PMF and the linear regression analyses indicates that the PMF solution is robust. While biomass burning is indeed  
33 a key source of aerosol, the study shows the presence of other important sources in the SCS/WPS. Identifying these sources is  
34 not only key for characterizing the chemical profile of the SCS/WPS but, by improving our picture of aerosol sources in the  
35 region, is also a step forward in developing our understanding of aerosol-meteorology feedbacks in this complex environment.

36

## 37 **1. Introduction**

38 In the midst of several developing countries, the South China Sea/West Philippine Sea (SCS/WPS) is a receptor for  
39 a multitude of natural and anthropogenic sources of aerosol. At the same time, the region exhibits some of the world's most  
40 complicated meteorology due to its archipelagic/peninsular terrain and strong Asian monsoon climate. Thus, the SCS/WPS  
41 hosts one of the world's most complex and sensitive composition and climate regimes (Balasubramanian et al., 2003; Yusef  
42 and Francisco, 2009; Atwood et al., 2013a, b; Reid et al., 2012, 2013, 2015). It is known to be impacted not only by dust  
43 storms and industrial pollution from China (Wang et al., 2011; Atwood et al., 2013a) but also by biomass burning emissions  
44 from the Maritime Continent (Balasubramanian et al., 2003; Lin et al., 2007; Cohen et al., 2010a, 2010b; Wang et al., 2011;  
45 Reid et al., 2013, 2015, 2016). The transport of such emissions is enabled by the long atmospheric residence times of fine  
46 particles (Cohen et al., 2010a), potentially creating regional and global concerns through their effects on radiative forcing  
47 (Nakajima et al., 2007; Boucher et al., 2013; Lin et al., 2013; Ge et al., 2014) and cloud properties (Sorooshian et al., 2009;  
48 Lee et al., 2012; Boucher et al., 2013; Ross et al., 2018).

49 Highlighting the unique combination of terrain and sea that feeds into the complexity of the meteorological  
50 environment of the region, Reid et al. (2012) and Xian et al. (2013) posed the long-range hypothesis that monsoonal flows and  
51 higher-frequency meteorological phenomena are a major factor in seasonal aerosol dispersion. Biomass burning plumes are  
52 known to cause severe haze episodes due to these monsoonal flows, raising concentrations of particulate matter (PM) to impact  
53 cloud physics and, in some cases, to dangerous air quality levels across large areas, particularly in association with positive  
54 phases of the El Niño-Southern Oscillation (ENSO) (Engling et al., 2014; Fujii et al., 2015). Likewise, biomass burning is a  
55 significant contributor to the region's cloud condensation nuclei (CCN) budget in all years as are the region's significant  
56 anthropogenic emissions (Balasubramanian et al., 2003; Field et al., 2008; Reid et al., 2012; 2013; 2015; 2016; Atwood et al.,  
57 2017).

58 Partly due to the emphasis on dramatic biomass burning as the primary source of aerosol particles in the region, the  
59 contributions of other regional sources are not well understood or perhaps underappreciated. As the SCS/WPS is host to major  
60 population centers, industry, major ports, and coal and oil combustion are expected to be an important regional source of  
61 aerosol particles in the MC. Coarse mode dust and biogenic particles may also play a role as ice nuclei (O'Sullivan et al.,  
62 2014), as biomass burning plumes are known to entrain such particles (Reid et al., 1998; 2005; Schlosser et al., 2017). As such,  
63 a network of interacting sources exists in the region surrounding the SCS/WPS, wherein aerosol particles mix during transport  
64 and complicate source apportionment. Understanding the nature of sources in the remote MC and their contributions is key to  
65 characterizing the aerosol environment in the SCS/WPS and its relationship with cloud behavior and precipitation patterns in  
66 the region; this is particularly true given the higher sensitivity of clouds to particle perturbations at lower concentrations.  
67 However, the source apportionment of aerosol particles is complicated by their complex chemistry and interactions with the  
68 marine environment (Atwood et al., 2013a; 2017).

69 As part of the Seven South East Asian Studies program (7-SEAS), a research cruise (Reid et al., 2015) was conducted  
70 in late September 2011 onboard the Philippine-flagged M/Y *Vasco* in the vicinity of the northern Palawan archipelago. The  
71 goal of this cruise was to observe the behavior of aerosol particles in the SCS/WPS and test the transport hypothesis proposed  
72 in Reid et al. (2012) that the Philippines is a long-range receptor of aerosol species transported across the SCS/WPS during  
73 the Asian summer monsoon from Borneo, Sumatra, and the Malay Peninsula. In particular, the cruise aimed to observe that  
74 emissions from the Maritime Continent were reaching the southwest monsoon trough. The Palawan archipelago is a good  
75 receptor site for regional emissions due to its largely rural settlements and its location upwind relative to the rest of the  
76 Philippines. The sampling period coincided with the passage of one tropical storm and two tropical cyclones (TC). Of particular  
77 importance is the passage of super typhoon Nesat beginning on 26 September 2011 as TC inflow arms are known to cause  
78 abrupt changes in regional flows.

79 As part of the 2011 *Vasco* cruise, particulate matter was collected using a size segregated Davis-Rotating Uniform  
80 Size-Cut Monitor (DRUM) impactor analyzed for elemental composition. While Reid et al. (2015) noted the presence of smoke  
81 plumes in two episodes during the cruise, their initial analysis of the region's atmospheric chemistry also suggested the events  
82 were a mix of biomass burning and oil or shipping emissions due to elevated levels of vanadium. Additionally, differences in  
83 elemental ratios, mass fractions and back trajectory origins between the two events support the presence of other sources  
84 besides biomass burning. From the initial analysis of aerosol chemistry presented by Reid et al. (2015), this study aims to  
85 identify aerosol sources in the SCS/WPS, to highlight the source variability present in the region, and to further develop the  
86 current understanding of the effect of regional meteorological phenomena on aerosol dispersion. The paper shows that, though  
87 biomass burning is a major source of aerosols in the SCS, anthropogenic sources such as oil combustion also play an important  
88 role in the chemical profile of the region. As we report, soil transport was observed as well.

89 In this paper we expand on the original 2011 *Vasco* cruise analysis to quantitatively apportion sampled biomass  
90 burning and anthropogenic aerosol species. Positive Matrix Factorization (PMF) was performed on size-segregated, elemental  
91 PM to detect possible size-specific sources (Han et al., 2006; van Pinxteren et al., 2016). Indeed, the relationship between the  
92 aerodynamic diameter of a particle and its source has been well-established in literature (Reid et al., 1993; Balasubramanian  
93 et al., 2003; Han et al., 2006; Lestari et al., 2009; Wimolwattanapun et al., 2010; Santoso et al., 2010; Karanisiou et al., 2009;  
94 Seneviratne et al., 2010; Atwood et al., 2013a; Lin et al., 2015; Cahill et al., 2016). Aerosol factors and characteristics were  
95 then used to spawn back trajectories to identify individual island emissions areas.

## 96 2. Sampling and Methods

### 97 2.1. Overall cruise sampling and environment

98 A general overview of the 2011 cruise can be found in Reid et al. (2015) and a brief summary is provided here.  
99 Sampling was conducted around the Palawan archipelago, an island chain located at the southwestern edge of the Philippines  
100 in between the SCS/WPS and the Sulu Sea. Sampling was performed between Manila and the northern tip of Palawan Island  
101 onboard the *M/Y Vasco* which left Manila Bay on 17 September 2011 and returned on 30 September 2011 (Fig. 1). Majority  
102 of samples were collected around the areas of El Nido and Malampaya Sound (111.1° N, 119.3° E) where the vessel was on  
103 station from 21-28 Sept. The largely rural population of Palawan made it an ideal receptor for regional rather than local  
104 emissions.



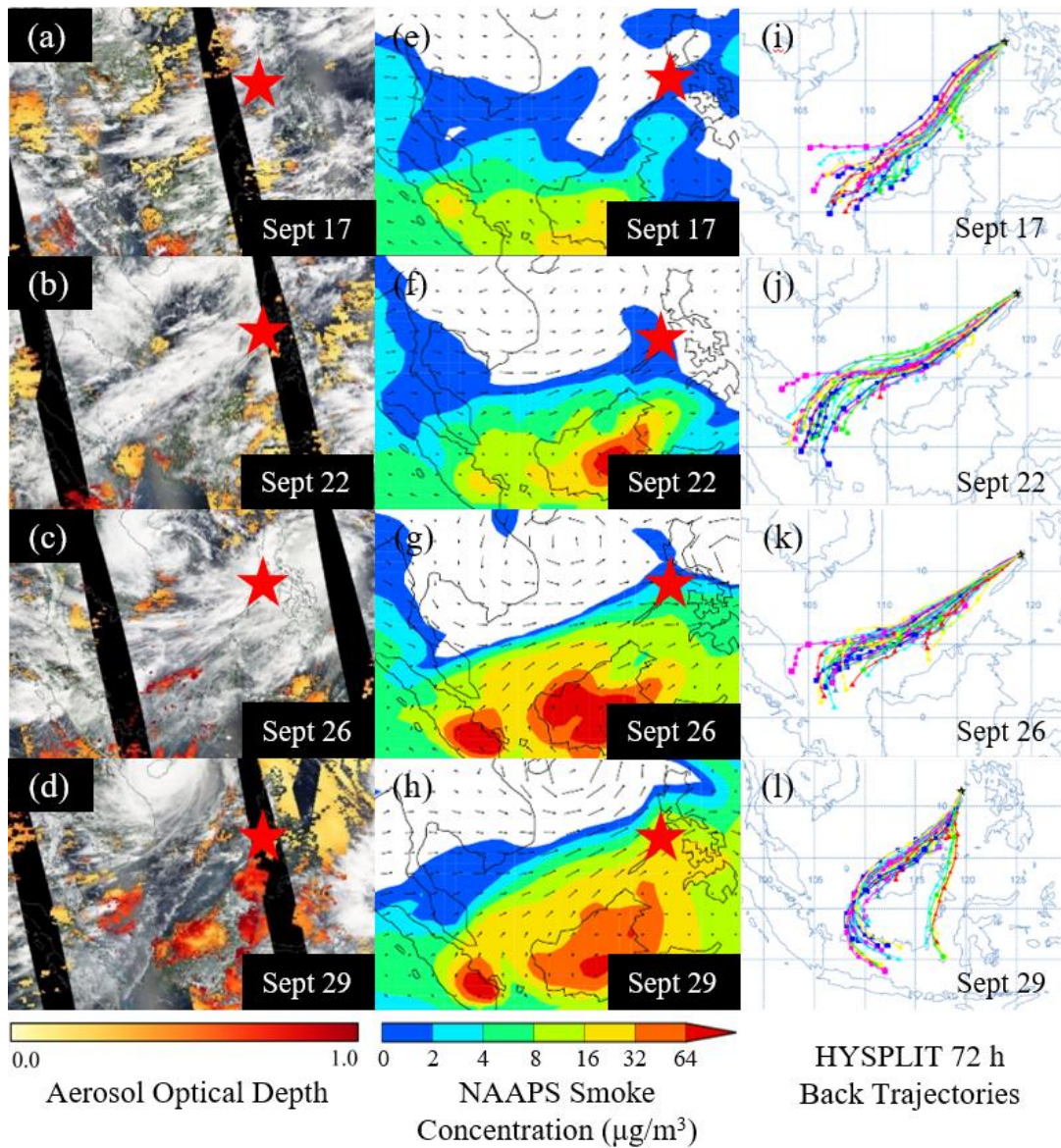
105  
106 **Figure 1. Path taken by the *M/Y Vasco* for 17-20 September (red), 20-28 September (black), 28-30 Sept (blue). Majority**  
107 **of sampling was done at the northern end of Palawan island. Image courtesy of Google Maps (map data ©2018 Google).**

108 The cruise was conducted at the end of the Asian summer monsoon which usually lasts from June through September  
109 (Loo et al., 2014; Chang et al., 2005). The Asian monsoon is caused by the annual march of the sun and asymmetrical heating  
110 of air masses due to the complex terrain of Southeast Asia (Chang et al., 2005). The campaign coincided with the peak burning  
111 season in Southern Kalimantan and Southern Sumatra, which have been measured to be the highest emitters of biomass burning  
112 plumes in the MC (Reid et al., 2012). As the southwest monsoon is characterized by winds travelling southwest to northeast,  
113 Reid et al. (2015) proposed that the Philippines was an excellent receptor for regional emissions from the MC.

114           Although 2011 was a moderate La-Niña year, it was noted that fire activity and precipitation levels resembled a  
115 neutral year (Reid et al., 2015). The cruise took place when the Madden-Julian Oscillation (MJO) was transitioning from the  
116 wet phase to the dry phase, which is expected to enhance burning activity and transport. With the passage of tropical cyclones  
117 (TCs), significant aerosol events were observed to propagate across the region.

118           Reid et al. (2015) described three tropical events that occurred during the cruise, specifically tropical storm (TS)  
119 Haitang, super-TC Nesat, and super-TC Nalgae. The presence of inflow arms in the SCS has been suggested to affect the  
120 aerosol environment by bringing more MC air into the region (Reid et al., 2015). The passage of Nesat was observed to abruptly  
121 affect air mass trajectories coinciding with an enhancement of several elements during the last two days of the cruise.

122           Figure 2 shows the evolution of the meteorological environment over the cruise period with comparisons between  
123 satellite-derived aerosol optical depth (AOD) derived from the Moderate Resolution Imaging Spectroradiometer (MODIS)  
124 onboard the Terra and Aqua satellites, back trajectories from NOAA Hybrid Single Particle Lagrangian Integrated Trajectory  
125 Model (HYSPPLIT) and 850 hPa smoke concentrations from the Navy Aerosol Analysis and Prediction System (NAAPS).  
126 Back trajectories were run for 72 hours ending at 00:00 Coordinated Universal Time (UTC)/08:00 Local Time (LT) and  
127 constrained to isobaric, 300m above ground level (AGL).



128

129 **Figure 2.** Satellite images of the SCS/WPS region taken from (a-d) NASA Worldview with overlaid AOD, (e-h) NAAPS  
 130 smoke concentration plots ( $\mu\text{g}/\text{m}^3$ ; 850 hPa) and (i-l) HYSPLIT ensemble back trajectories during the cruise for 18, 22,  
 131 26 and 29 Sept (isobaric; 300m AGL; 72 hours; ending at 00:00 UTC/08:00 LT). Red star indicates location of the  
 132 *Vasco*.

133 **2.2. Aerosol sampling and analysis**

134 Size-resolved aerosol samples were collected during the cruise using a Davis-Rotating Unit for Monitoring (DRUM)  
 135 continuously sampling cascade impactor. Samples were collected with a  $10 \mu\text{m}$  inlet and eight size cuts at 5, 2.5, 1.15, 0.75,  
 136 0.56, 0.34, 0.26,  $0.10 \mu\text{m}$  at a 90-minute time resolution from noontime 17 September until noontime 30 September local-time.  
 137 Particles were collected on Mylar strips coated with Apiezon grease. The eight drums were rotated at a consistent rate to create  
 138 a temporal record of mass concentration (Raabe et al., 1988). X-ray fluorescence (XRF) was performed on the DRUM samples  
 139 at the Advanced Light Source (ALS) of Lawrence Berkeley National Laboratory to measure mass concentrations of 28  
 140 elements ranging from Na to Pb. In this study, data was filtered based on location notes from the cruise such that samples

141 collected in the vicinity of Manila Bay were excluded from the analysis. Additionally, samples during an 8-hour pump failure  
142 that occurred on 20 September were also excluded from the dataset. In the analysis, the stages were aggregated into three  
143 modes: coarse (1.15-10  $\mu\text{m}$ ), fine (0.34-1.15  $\mu\text{m}$ ) and ultrafine (0.10-0.34  $\mu\text{m}$ ) modes. A large difference in the concentrations  
144 of stage 6 (0.34-0.56  $\mu\text{m}$ ) compared to adjacent stages 5 (0.56-0.75  $\mu\text{m}$ ) and 7 (0.26-0.34  $\mu\text{m}$ ) was observed. The sharp decrease  
145 in concentrations in stage 6 despite the high concentrations in stages 5 and 7 has been observed in other studies involving the  
146 DRUM sampler; this is likely due to DRUM sampling artifacts and does not reflect the true aerosol mass distribution (Atwood  
147 et al., 2013a). Nevertheless, the two size resolved modes lend themselves to size segregated analysis. In this study, we simply  
148 report the mass distributions as sampled by the DRUM.

149 In addition to the DRUM sampler, eight sets of  $\text{PM}_{2.5}$  filters were collected during the cruise and were chemically  
150 analyzed for information on species such as sulfate, nitrate, and organic carbon. The  $\text{PM}_{2.5}$  filters were described more fully in  
151 Reid et al. (2015). Mass reconstruction was performed on the  $\text{PM}_{2.5}$  filter data according to the methodology of Malm and  
152 Hand (2007). Results are shown in Fig. S1 and discussed briefly in Section 3.1.

### 153 **2.3. Model and satellite data**

154 NOAA Hybrid Single Particle Lagrangian Integrated Trajectory Model (HYSPLIT) back trajectories (Draxler et al.,  
155 1998, 1999) were generated throughout the cruise period to investigate locations of aerosol emission. HYSPLIT back  
156 trajectories have been used in several studies to establish air mass source regions (Lin et al., 2007; Cohen et al., 2010a; Atwood  
157 et al. 2013a, 2017). Back trajectories were run for 72 hours for heights of 500 m and 300 m to investigate possible vertical  
158 inhomogeneity that has been noted in other SCS/WPS papers (Atwood et al., 2013a). Trajectory endpoints corresponded to  
159 cruise coordinates. Trajectories were constrained isobarically to limit vertical wind velocity since our area of interest is surface-  
160 level emission.

161 The Navy Aerosol Analysis and Prediction System (NAAPS) reanalysis product (Lynch et al., 2016) with driving  
162 meteorology from the Navy Global Environmental Model (NAVGEM) was used to provide overall aerosol and meteorological  
163 context to the analysis. This reanalysis utilizes a modified version of the NAAPS as its core and assimilates quality controlled  
164 retrievals of aerosol optical depth (AOD) from MODIS on Terra and Aqua and the Multi-angle Imaging SpectroRadiometer  
165 (MISR) on Terra (Zhang et al., 2006; Hyer et al., 2011; Shi et al., 2014). NAAPS characterizes anthropogenic and biogenic  
166 fine (including sulfate, and primary and secondary organic aerosols), dust, biomass burning smoke and sea salt aerosols. Smoke  
167 from biomass burning is derived from near-real time satellite based thermal anomaly data to construct smoke source functions  
168 (Reid et al., 2009), with additional orbital corrections on MODIS based emissions and regional tunings. The system has been  
169 successfully used to monitor biomass burning plumes and to study the relationship of aerosol lifecycle to weather systems over  
170 the MC (Reid et al., 2012, 2015, 2016; Atwood et al., 2013b; Xian et al., 2013).

171 Active fire hotspot data was downloaded from the Fire Information for Resource Management System (FIRMS)  
172 (<https://firms.modaps.eosdis.nasa.gov/>). Active fire hotspots and aerosol optical depth (AOD) at a wavelength of 550 nm were  
173 tracked throughout the cruise via MODIS. MODIS detects thermal anomalies across a region to identify possible fire activity.  
174 MODIS-derived AOD was used to derive large-scale estimates of PM<sub>2.5</sub> in some studies (e.g., Zheng et al., 2017). In the study,  
175 MODIS was used to track burning emissions which were found to be particularly prevalent in Eastern Malaysia and Indonesia.  
176 The use of MODIS to track active fire hotspots has been used in other studies to understand seasonal trends in agricultural  
177 burning (Reid et al., 2012) and to identify and locate burning-related sources when used in conjunction with HYSPLIT back  
178 trajectories (Atwood et al., 2017).

179 The NASA Worldview site ([www.worldview.nasa.gov](http://www.worldview.nasa.gov)), an application operated by the NASA/Goddard Space Flight  
180 Center Earth Science Data and Information System (ESDIS) project, was used to supplement the satellite data by providing  
181 true color images of the region and is particularly useful in demonstrating sudden changes of cloud environment or monsoon  
182 flow caused by tropical cyclones.

#### 183 **2.4. Positive Matrix Factorization**

184 Positive Matrix Factorization (PMF) was used to study the covariance of elemental species. PMF is a multivariate  
185 factor analysis technique used in source apportionment that resolves a sample matrix  $\mathbf{X}$  ( $i \times j$ ) of  $i$  samples and  $j$  species into  
186 matrices  $\mathbf{G}$  ( $i \times k$ ),  $\mathbf{F}$  ( $k \times j$ ), and  $\mathbf{E}$  ( $i \times j$ ), the source contribution matrix, source profile matrix and residual matrix,  
187 respectively, with the assumption of  $k$  factors:

$$188 \quad X_{ij} = G_{ik}F_{kj} + E_{ij}$$

189 The goal of PMF is to determine the number of factors or sources  $k$  such that the solution will be physically interpretable.  
190 Developed by Paatero and Tapper (Paatero and Tapper, 1994), PMF is a well-established approach used in previous source  
191 apportionment studies (Polissar et al., 1998; Lee et al., 1999; Han et al., 2006; Chan et al., 2008; Karanisiou et al., 2009; Lestari  
192 et al., 2009; Santoso et al., 2010; Wimolwattanapun et al., 2010). PMF provides more physically realistic results compared to  
193 other factor analysis techniques due to non-negative constraints in the model and better treatment of missing or below detection  
194 limit (BDL) values by increasing the associated uncertainty (Paterson et al., 1999).

195 PMF outputs source profiles ( $F$ ) and source contributions ( $G$ ). PMF source profiles were normalized to the percent of  
196 species sum, defined as the percent concentration of an element apportioned to a source. An outlier threshold distance  $\alpha$  was  
197 used to reduce the effect of extremely large data points and was set at a value of 4.0 to be consistent with other PMF studies  
198 (Lee et al., 1999; Han et al., 2006).

199 Prior to analysis via PMF, the 28 elements measured via XRF were filtered based on their Pearson's R correlation with  
200 the total elemental PM mass per mode in order to improve the interpretability of PMF factors. A minimum Pearson's R value



201 of 0.0 was used, which removed elements that were negatively correlated with the total elemental PM. From the 28 elements  
202 identified by XRF, 20 elements in the coarse mode, 22 elements in the fine mode, and 19 elements in the ultrafine mode were  
203 included in the PMF analysis. Comparing profiles with and without the correlation-based filtering, there was no significant  
204 change in factor interpretation. This indicates that the removed elements were unnecessary for improving the PMF results  
205 (Liao et al. 2019; Ma et al., 2019). Tables S1-3 (Supplementary material) show the correlation coefficients of coarse-, fine-,  
206 and ultrafine-mode elements. The filtering of elements through correlation with total PM per mode was observed to improve  
207 the interpretability of the PMF outputs and remove the need for the matrix rotation parameter,  $F_{\text{peak}}$ .

208 Data screening was performed based on the approach of Polissar et al. (1998) and Han et al. (2006) to ensure that no  
209 erroneous data points were included in the analysis. BDL values were replaced by half the detection limit and relative  
210 uncertainties were set to 100% (Han et al., 2006). Signal-to-noise ratios were determined and elements with low ratios (less  
211 than 0.2) were excluded from the data set (Paatero and Hopke, 2003). Measured elemental concentrations below the detection  
212 limit of XRF were replaced with half the detection limit and their relative uncertainties were set to 100% as done in Han et al.  
213 (2006). Detection limit values and error values were based on values provided by the Lawrence Berkeley National Laboratory.

214 The current study employs a size-resolved PMF approach as a supplement to the other analysis methods. PMF is a  
215 powerful tool that quantifies the contributions of PM sources and is useful for forming an initial understanding of the possible  
216 sources from the data. However, PMF may neglect important events, particularly short-term ones, that can reveal insightful  
217 interactions between identified sources and is unable to dissociate covarying sources as it assumes orthogonality between  
218 factors (Van Pinxteren et al., 2016).

219 For this study, we included only the DRUM elemental data for PMF analysis. Speciated data from the  $\text{PM}_{2.5}$  filter was  
220 excluded due to the limited number of filters available (eight quartz and eight Teflon filters). The much higher temporal  
221 resolution (174 timestamps) from the DRUM sampler, in addition to its collection across eight size ranges, provided the  
222 necessary data resolution for PMF while offering the additional degree of freedom of size-resolved collection. Due to the  
223 limitations inherent in a two-week-long research cruise, the collected dataset is not expected to provide a full quantitative  
224 inventory of sources but rather provides an opportunity to study short-term aerosols events to gain a better understanding of  
225 source variability in the SCS region.

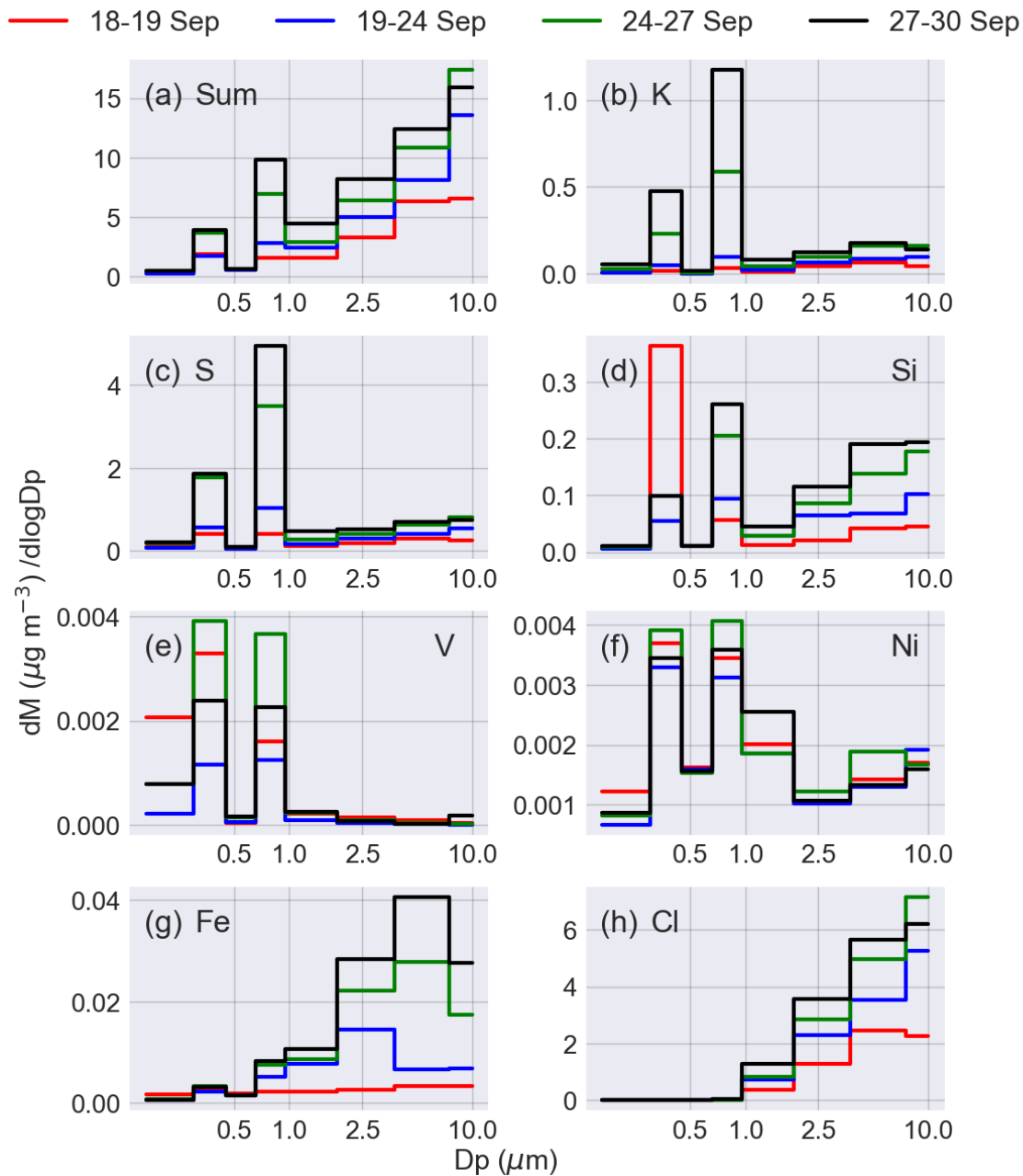
### 226 **3. Results I: Mass distributions and time series of selected elements**

#### 227 **3.1. Reconstructed mass and DRUM mass distributions**

228 Mass reconstruction performed on the  $\text{PM}_{2.5}$  filters shows an increasing trend in aerosol loadings towards the end of the  
229 cruise (Fig. S1a). A large event beginning on 28 Sept is characterized by heightened contributions of particulate organic matter.  
230 A smaller aerosol event was also detected by the 23 Sept and 25 Sept filters. The mass reconstruction shows that 53% of the

231 total  $PM_{2.5}$  gravimetric mass is accounted for by the reconstructed components which include organic carbon (Fig. S1b). The  
232 elemental contribution to the total  $PM_{2.5}$  mass was estimated as the summed contributions of the reconstructed sulfate, sea salt,  
233 and soil components according to formulas from Malm and Hand (2007) and Chow et al. (2015). Reconstructed elemental  
234 components derived from the DRUM sampler compose 21.2% of the total  $PM_{2.5}$  mass. This is approximately twice the value  
235 calculated with filter-collected elemental concentrations (11.7%).  $PM_{2.5}$  Teflon filters have been observed to show lower  
236 concentrations than rotating drum impactors for several elements, attributed to insufficient background subtractions when  
237 computing for filter concentrations (Venecek et al., 2016). Other potential factors in this discrepancy include a complicated  
238 sampling environment that may result in filter losses during collection and the long filter collection times during the cruise.

239 Elemental mass size distributions show normalized species concentrations ( $dM/d\log D_p$ ) across all eight DRUM stages  
240 and can be used to validate the signal of a mode-specific tracer. In addition to isolating the signal of a tracer, changes in the  
241 mass distributions of key elements over time indicate periods when mode-specific sources are present. Figure 3 depicts the  
242 mass size distributions of the (a) summed elemental PM, and key elements (b) potassium (K) as a tracer for biomass burning  
243 in the fine and ultrafine modes; (c) sulfur (S), a general indicator of combustion; (d) silicon (Si) for soil dust; (e) vanadium  
244 (V) and (f) nickel (Ni), which are often paired as tracers of oil combustion; (g) iron (Fe), another key tracer for dust; and (h)  
245 chlorine (Cl), a reasonable tracer for sea spray given the sampling location. Figure 3 is further divided into time periods,  
246 distinguished by color: 18-19 September (red), 19-24 September (blue), 24-27 September (green) and 27-30 September (black).



247

248 **Figure 3. Time evolution of mass size distributions over the cruise period. (a) Sum of all measured elements, (b)**  
 249 **potassium, (c) sulfur, (d) silicon, (e) vanadium, (f) nickel, (g) iron, and (h) chlorine. Time periods are colored: 18-19**  
 250 **Sept (red), 19-24 Sept (blue), 24-27 Sept (green), 27-30 Sept (black). Stage numbers are depicted in (a).**

251

252 The mass distribution of summed elemental PM (Fig. 3a) is informative as it shows distinct peaks in the coarse and  
 253 submicron ranges, pointing to a combustion or anthropogenic signal during the cruise. The total mass size distribution shows  
 254 that, over time, a regime-change occurred around 24 Sept during which the general back-trajectory origin shifts to the Maritime  
 255 Continent. Comparing the magnitude of the summed mass distribution to those of the key species, it is clear that S contributed  
 256 a significant part of the submicron mass. Elements associated with combustion showed peaks in stage 5 (0.56-0.75  $\mu\text{m}$ ) and  
 257 stage 7 (0.26-0.34  $\mu\text{m}$ ). K, S, and Si have very similar changes in their mass size distributions over the cruise period which are

258 suggestive of a common source (Fig. 3b-d). During the latter half of the cruise, a regime shift occurred wherein back-trajectory  
259 origins shifted to southern Kalimantan (Fig. 2). We observe coincident enhancements in K, S, and Si – indicative of a common  
260 source, likely biomass burning. These elements have strong peaks in stages 5 and 7 during the whole cruise but particularly  
261 high values are observed during the last days of the sampling period (27-30 Sept). A general enhancement late in the cruise is  
262 likely related to the increase in the number of active fire hotspots reported by Reid et al. (2015), who attributed these hotspots  
263 primarily to Indonesian Kalimantan and Southern Sumatra. As the cruise took place during the end of the Asian summer  
264 monsoon, 300 m AGL winds were predominantly southwesterly. A shift in back trajectories at the end of the cruise to the  
265 western and southern coasts of Borneo is observable in Fig. 2l, suggesting the source of the late-cruise enhancement to be the  
266 MC, which hosts elevated aerosol background levels during this time of year from seasonal burning (Reid et al., 2013). The  
267 advection of this large aerosol event can be observed in the NAAPS smoke model over the region (Fig. 2g, h). The attribution  
268 of late-cruise aerosol enhancement to the MC is in agreement with Reid et al. (2015) who noted that the AOD maps and  
269 southwesterly flows towards the end of the cruise were suggestive of southwesterly transport from the MC to SCS/WPS.

270 Covariance of Si (Fig. 3d) with K and S suggest possible fine soil entrainment caught in burning updraft (Reid et al.,  
271 2015). The stage 5 and stage 7 peaks in S are similar to those observed for northern SCS/WPS in the springtime (Atwood et  
272 al., 2013a); however, we report enhanced values, attributed to the timing of the sampling period during the MC burning season.

273 Interestingly, Si shows a strong peak early in the cruise (18-19 Sept) unique to the ultrafine mode which indicates this  
274 particular signal may not originate from soil dust but fly ash (Xie et al., 2009). As the *Vasco* was travelling past the islands of  
275 Mindoro and Coron en-route to Palawan, local sources are likely the cause of the ultrafine Si enhancement. This early-cruise  
276 Si signal is further examined through later time series and regressions.

277 V shows a mass distribution characteristic of a combustion source with strong peaks in stage 5, stage 7, and stage 8 (0.10-  
278 0.26  $\mu\text{m}$ ) (Fig. 3e). Almost no contribution was observed for coarser stages 1 through 4 (0.75 -10  $\mu\text{m}$ ), indicating that V did  
279 not originate from soil (Lin et al., 2015) and can be treated as a tracer for oil combustion. Ni shows a similar mass distribution  
280 (Fig. 3f) but had a larger spread over the eight stages than V, which may be due to contributions from other sources such as  
281 fly ash (Davison et al., 1974).

282 Fe and Cl, well-known tracers for soil dust and sea spray, respectively, showed coarse-mode distributions that taper off  
283 considerably in the submicron stages (Fig. 3g, h). Cl shows a purely coarse distribution, indicative of the influence of sea spray  
284 considering the sample location (Viana et al., 2008; Gugamsetty et al., 2012; Farao et al., 2014). Fe shows small peaks in stage  
285 4 (0.75-1.15  $\mu\text{m}$ ), stage 5, and stage 7; however, these do not constitute a significant signal relative to its coarse mode  
286 concentrations. As such, we treat Fe as our coarse mode soil dust tracer. The mass distribution of Fe is observed to increase  
287 across stages 1 through 3 (2.5-10  $\mu\text{m}$ ) over the cruise period. The increase in coarse Fe coincides with the NAAPS-simulated  
288 transport of smoke (Fig. 2g, h) and mirrors the enhancements of K, S, Si (Fig. 4a, b), and Al (Fig. S2a, b). These patterns

289 suggest that coarse soil dust accompanies smoke emissions, possibly through entrainment. The presence of soil dust is further  
290 corroborated by Fig. 3d, which show the presence of Si in the coarse mode. The distinct coarse and fine mode peaks of Al and  
291 Si indicate separate soil dust sources. As fine mode particles have longer residence times (Cohen et al., 2010a), the fine peaks  
292 may be an indicator of long-range transport of fine soil dust through the SCS/WPS.

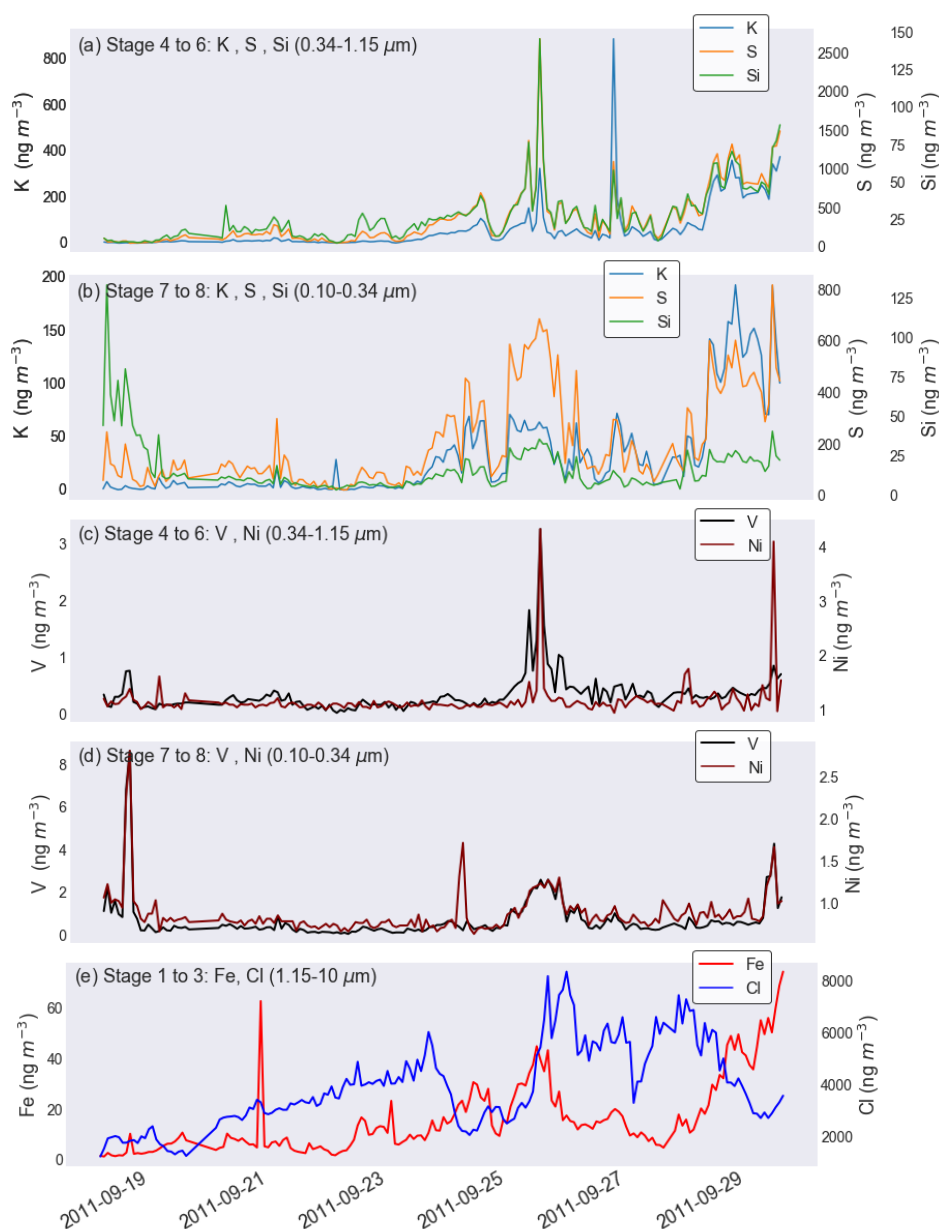
293 Interpreting DRUM data reveals insights about the composition and interpretation of sources. Table 1 shows the ratios  
294 of elemental  $PM_{1.15}/PM_{10}$  mass concentrations. As in Atwood et al. (2013a), the ratio-slope was computed by taking the slope  
295 of the linear regression line between elemental  $PM_{1.15}$  and  $PM_{10}$  mass concentrations, accompanied by  $r^2$  values. Direct  
296 averages of per-timestamp ratios of  $PM_{1.15}$  and  $PM_{10}$  were also taken to compute for ratio-averages, accompanied by the  
297 standard deviation of the ratios. Fe and Cl both had ratios of 0.06, which confirm the predominantly coarse nature of these  
298 species. As commonly used tracers of soil dust, Al and Si show moderate ratio-slope values of 0.51 and 0.29, respectively,  
299 suggesting that Al resides in both coarse and fine ( $PM_{1.15}$ ) modes while Si is predominantly coarse. As expected, elements  
300 commonly associated with anthropogenic species such as V, K, and S show high  $PM_{1.15}/PM_{10}$  ratios (0.8 and above) which  
301 indicate that these elemental particles largely reside in the fine and ultrafine modes. The high ratios of V, K, and S provide  
302 evidence for the presence of anthropogenic emissions from sources such as oil combustion and biomass burning while the low  
303 ratios of Fe and Cl support their treatment as tracers for soil dust and sea spray, respectively.

304 The time-resolved DRUM data is important for showing variations in species which may be representative of  
305 important aerosol events. Thus, observations on the time-resolved DRUM data can aid in our analysis. At the beginning of the  
306 cruise, between 18 to 19 Sept, V, Ni, and Si show enhancements in stages 5, 7, and 8. The stage 7 Si peak during this time is  
307 the maximum concentration over the entire cruise period, so this warrants further analysis through later time series and  
308 regressions. The period of 19-24 Sept shows a low point in the DRUM peaks of several elements, most notably combustion  
309 tracers K and V (Fig. 3b, e), while Cl (Fig. 3h) shows higher peaks in the coarse-mode which suggests a period of clean marine  
310 aerosol. This period was described by Reid et al. (2015) as the cleanest of the cruise. The NAAPS model shows nearly zero  
311 smoke concentration at the sampling site (Fig. 2f) while 72-h HYSPLIT back trajectories indicate that air masses originate  
312 from central SCS/WPS (Fig. 2j). From 24 to 27 Sept, we observed the first major aerosol event characterized by the stage 5  
313 and 7 enhancements of several combustion elements: K, S, Si, V, and Ni (Fig. 3b-f). Fe, our coarse-mode soil dust tracer,  
314 shows enhancements in stages 1 to 3 (Fig. 3g), which points to combustion-related entrainment of soil dust in the coarse mode.  
315 The NAAPS model (Fig. 2g) depicts the intensification and spread of a smoke-related aerosol event that had been escalating  
316 in southern Kalimantan since 22 Sept, reaching the *Vasco* around 26 Sept. During this mid-cruise period, concentrations of  
317 biomass burning species K, S, Si, Al are elevated, and oil combustion tracers V and Ni show their maximum concentrations  
318 for the cruise in stages 5 and 7 (Fig. 4e, f). The last period, 28 to 30 Sept, depicts the highest concentrations of elements  
319 associated with biomass burning (Fig. 4a, b; Fig. S2a, b). As seen in the NAAPS smoke model (Fig. 2h) and HYSPLIT model  
320 (Fig. 2l), the westward movement of TC Nesat across the region alters back trajectories to wind around Borneo island, reaching

321 southern Kalimantan which hosted a high active fire hotspot density during the time (Reid et al., 2015), thus bringing polluted  
 322 air masses toward the sampling site. Stage 5 and 7 peaks of K and S are quite notable as no other stages show significant  
 323 enhancements in response to this event. Fe and Si show similar changes but for the coarser stages 1 to 3 (Fig. 3d, g), indicating  
 324 a covariance of soil dust and biomass burning tracers. The temporal trends from the DRUM data serve as an entry point into  
 325 the time series analysis. By identifying key DRUM stages and time periods per element based on their mass size distributions,  
 326 we can then examine these stages to observe aerosol events over the cruise period.

### 327 3.2. Time series of selected elements

328



329 **Figure 4. Time series of (a) Stage 4-6 K, S, Si, (b) Stage 7-8 K, S, Si, (c) Stage 4-6 V, Ni, (d) Stage 7-8 V, Ni, and (e) Stage**  
 330 **1-3 Fe, Cl.**

331 The first few days of the cruise showed an 18 Sept event in oil combustion tracers V and Ni in the ultrafine mode (Fig.  
332 4d) with a coincident but lower-magnitude response in the fine mode (Fig. 4c). Ultrafine mode V and Ni show their maxima  
333 for the cruise period during this time, expanded further in Section 5. High concentrations of ultrafine Si were sampled during  
334 this time from the beginning of the cruise until 19 Sept when it dropped to stable background levels. This early-cruise  
335 enhancement was also seen in its mass distribution plot (Fig. 3d). As the *Vasco* was traveling among islands, the Si signal may  
336 be due to local sources en-route to the El Nido sampling site.

337 Reid et al. (2015) noted periods of clean regime after departing Manila Bay through midday 22 Sept, observable in the  
338 consistently low concentrations of various elements (Fig. 4). Chlorine shows a gradual increase in concentration from 20 Sept  
339 until 24 Sept. Chlorine, although it ages into HCl, is assumed to be fresh due to the sampling location and can therefore be  
340 used as an indicator of sea spray. Interestingly, coarse-mode Cl (Fig. 4e) showed peak concentration times during low points  
341 in the concentrations of anthropogenic aerosol species (Fig. 4a-d), marking periods of clean marine aerosol on 22-24 Sept and  
342 26-28 Sept. Wet deposition processes are likely responsible for the suppressed anthropogenic aerosol concentrations as  
343 precipitation was prevalent during these periods (Reid et al., 2015). Conversely, peaks in the concentrations of anthropogenic  
344 aerosol occurred during dry periods of the cruise when precipitation was low: 24-26 Sept and 28-30 Sept. During the periods  
345 of clean marine aerosol, back trajectories shift away from source regions and traverse open sea (Fig. 2j, k) which also hosts a  
346 lower shipping route density compared to coastal regions (Fig. S3, Supplementary material). The first half of the cruise also  
347 saw the lowest concentrations from species associated with biomass burning, specifically submicron K, S, Si, (Fig. 4a, b), and  
348 Al (Fig. S2a, b, Supplementary material). These species track each other quite well throughout the cruise period indicating a  
349 common source.

350 The event between 24 Sept and 26 Sept is observable on the time series of several key elements. The plume was the first  
351 of two distinct plume events reported by Reid et al. (2015) with the later plume occurring on 29 Sept. The enhancement of all  
352 elements in Fig. 4 suggests a mix of biomass burning, oil combustion and soil dust influences within the 24-26 Sept plume.  
353 Fine mode V and Ni show their maximum concentrations for the cruise during this event (Fig. 4c). Although these two plumes  
354 appeared as one uniform progression across the SCS/WPS region on the NAAPS smoke model (Fig. 2h), the time series  
355 showed the presence of two distinct events (Fig. 4), which is corroborated by observations from Reid et al. (2015). During this  
356 period, aerosol concentrations dropped sharply before recovering due to the passage of squall lines, observed in the time series  
357 for K, S, Si, Fe, and Cl (Fig. 4a, b, e). As concluded in Reid et al. (2015), frequent, short-term events such as cold pools and  
358 squall lines must be accounted for in modeling studies in order to properly capture aerosol-convection interaction.

359 The period between plumes (26-28 Sept) is characterized by an overall drop in the aerosol concentration of species  
360 associated with anthropogenic sources (K, S, V, Ni; Fig. 4a-d). As Cl concentrations show peak values during this period (Fig.  
361 4d), this indicates a period of pure marine aerosol sampling similar to the 22-24 Sept clean period. Coinciding with the passage

362 of TC Nesat through the SCS/WPS, the observed drop in aerosol concentration is attributed to a possible restriction of shipping  
363 traffic in response to the TC and scavenging of aerosols by precipitation along the TC inflow arm (Fig. 2c) (Reid et al., 2015).

364 The last days of the cruise were particularly eventful as the largest aerosol event of the cruise period was visible on the  
365 NAAPS model in the form of smoke (Fig. 2h), accompanied by the spread of high AOD values throughout the SCS/WPS (Fig.  
366 2d). Although the large areas of cloud cover created by TC Nesat hinders the detection of AOD on 26 Sept, the region is free  
367 of cloud cover by 29 Sept that significant AOD values were observed to visibly stretch from Southern Kalimantan towards the  
368 *Vasco* sampling site (Fig. 2d). In general, the NAAPS smoke transport model agrees with the spatial distribution of high AOD.  
369 Here, NAAPS modelling of smoke transport is useful in demonstrating the event's northward advection and the severity of  
370 smoke concentration in Borneo island on 26 Sept (Fig. 2h). Time series plots of elements associated with biomass burning (K,  
371 S, Si; Fig. 4a, b) and coarse mode soil dust (Fe; Fig. 4d) show significant enhancements during this time which were also  
372 observed on their mass distributions (Fig. 3). HYSPLIT back trajectories show that air masses originate from Southern  
373 Kalimantan during this period as opposed to mainland Malaysia during the first half (Fig. 2j, l). The shift in air mass trajectories  
374 is attributed to the passage of TC Nesat through the region as inflow arms from TCs have been observed to accelerate air mass  
375 advection across the SCS/WPS, bringing more MC air into the region (Reid et al., 2012; 2015). The observed transport of  
376 emissions from Borneo indicates that TC-enhanced long-range transport is a significant factor in SCS/WPS aerosol dispersion.

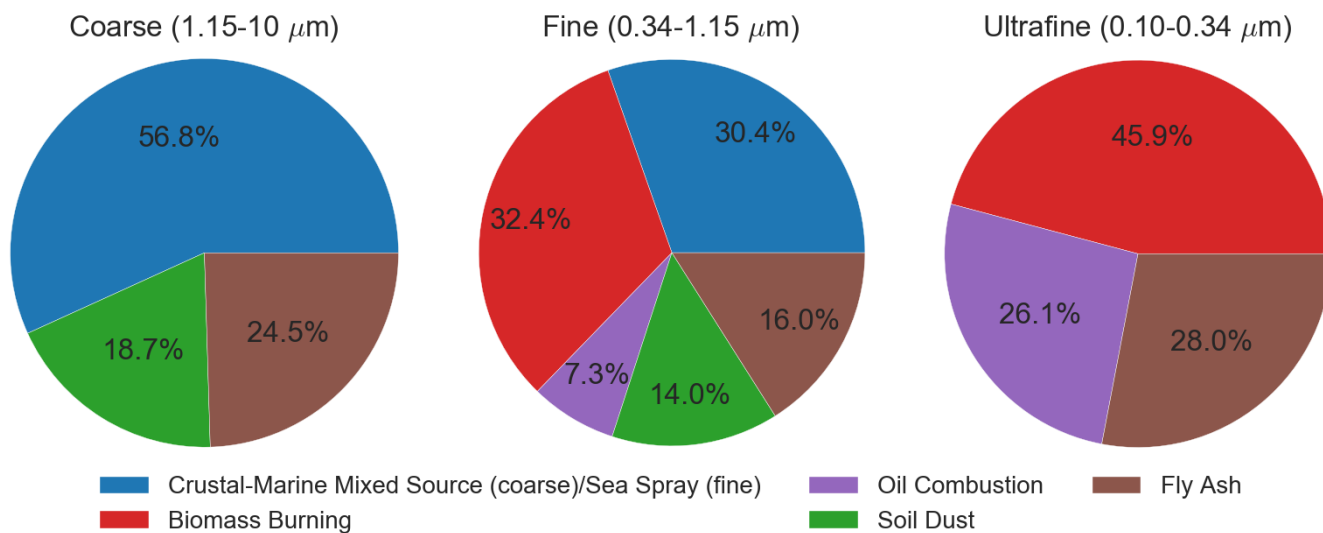
## 377 **4. Results II: positive matrix factorization and regressions**

### 378 **4.1. Source apportionment via positive matrix factorization**

379 To verify groupings of key elements and aid in source identification, size-resolved PMF was performed. As described in  
380 Section 2, the eight-stage DRUM data were combined into coarse (1.15-10  $\mu\text{m}$ ), fine (0.34-1.15  $\mu\text{m}$ ) and ultrafine (0.10-0.34  
381  $\mu\text{m}$ ) modes and the species included in the PMF analysis were then filtered based on their correlation to the aggregated PM  
382 concentration per mode. The PMF analysis resolved six sources across the three size ranges: biomass burning, oil combustion,  
383 soil dust, a crustal-marine mixed source, sea spray, and fly ash (Table 2). Due to the similarities in composition and temporal  
384 trends of the crustal-marine mixed source in the coarse mode and the sea spray factor in the fine mode, they are depicted  
385 together in Fig. 5-7 for simplicity.

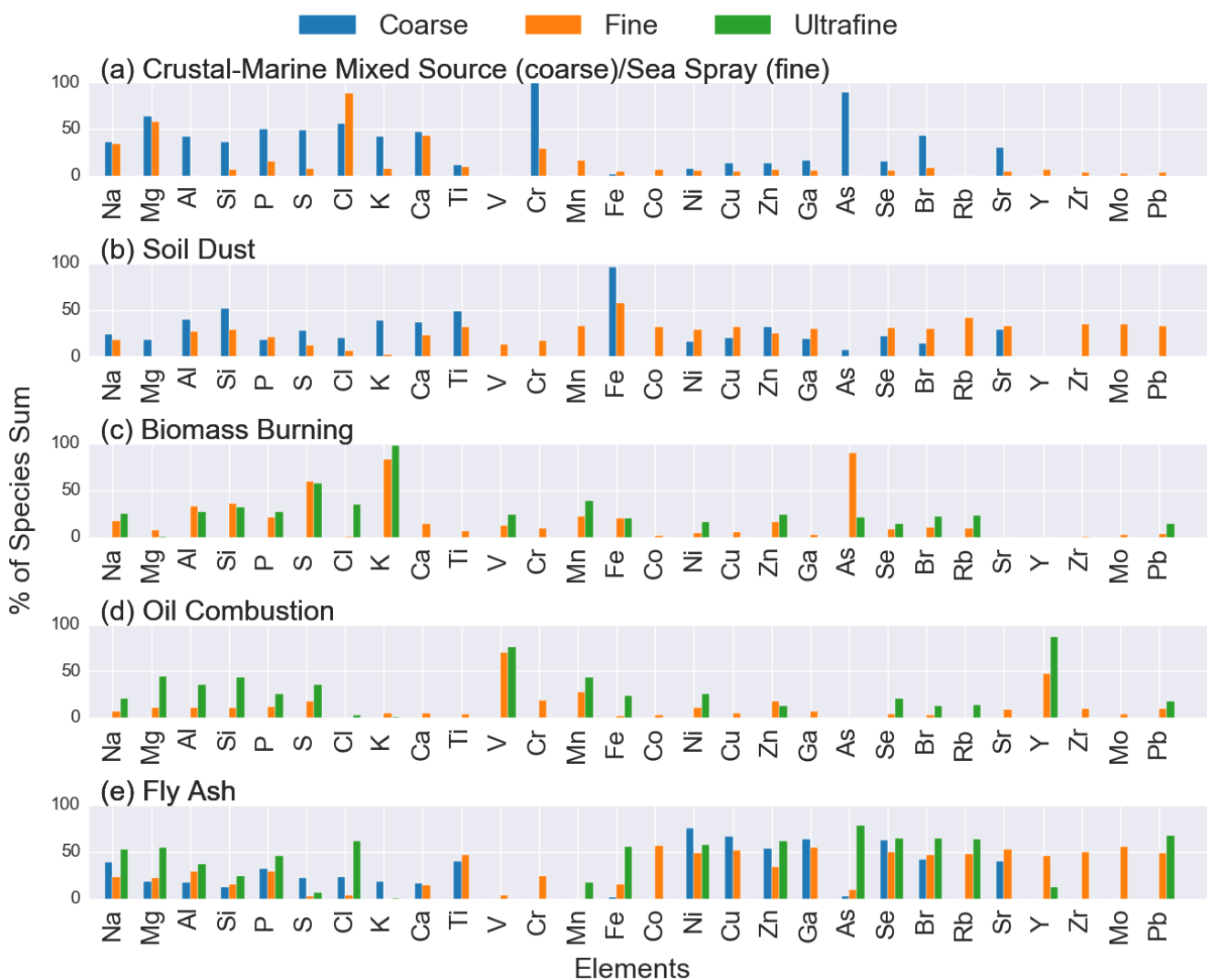
386 One strength of PMF is its quantification of a source's contribution. Figure 5 shows the percent contribution of each source  
387 relative to the total elemental PM mass. As expected, natural sources such as the crustal-marine mixed source and soil dust  
388 mainly contribute to the coarse mode while combustion-related sources such as biomass burning and oil combustion contribute  
389 to the fine and ultrafine modes. The identification of sea spray in the fine mode is likely due to the existence of Cl in stage 4  
390 of the DRUM sampler (Fig. 3h). The existence of these sources in their expected modes is an indicator of the successful  
391 implementation of PMF. The following sections describe the observed characteristics of sources determined by PMF.





392

393 **Figure 5. Contributions of factors to the total elemental PM mass. The crustal-marine mixed source (coarse mode) and**  
 394 **sea spray (fine mode) share the same color to reflect their similar chemical compositions.**



395

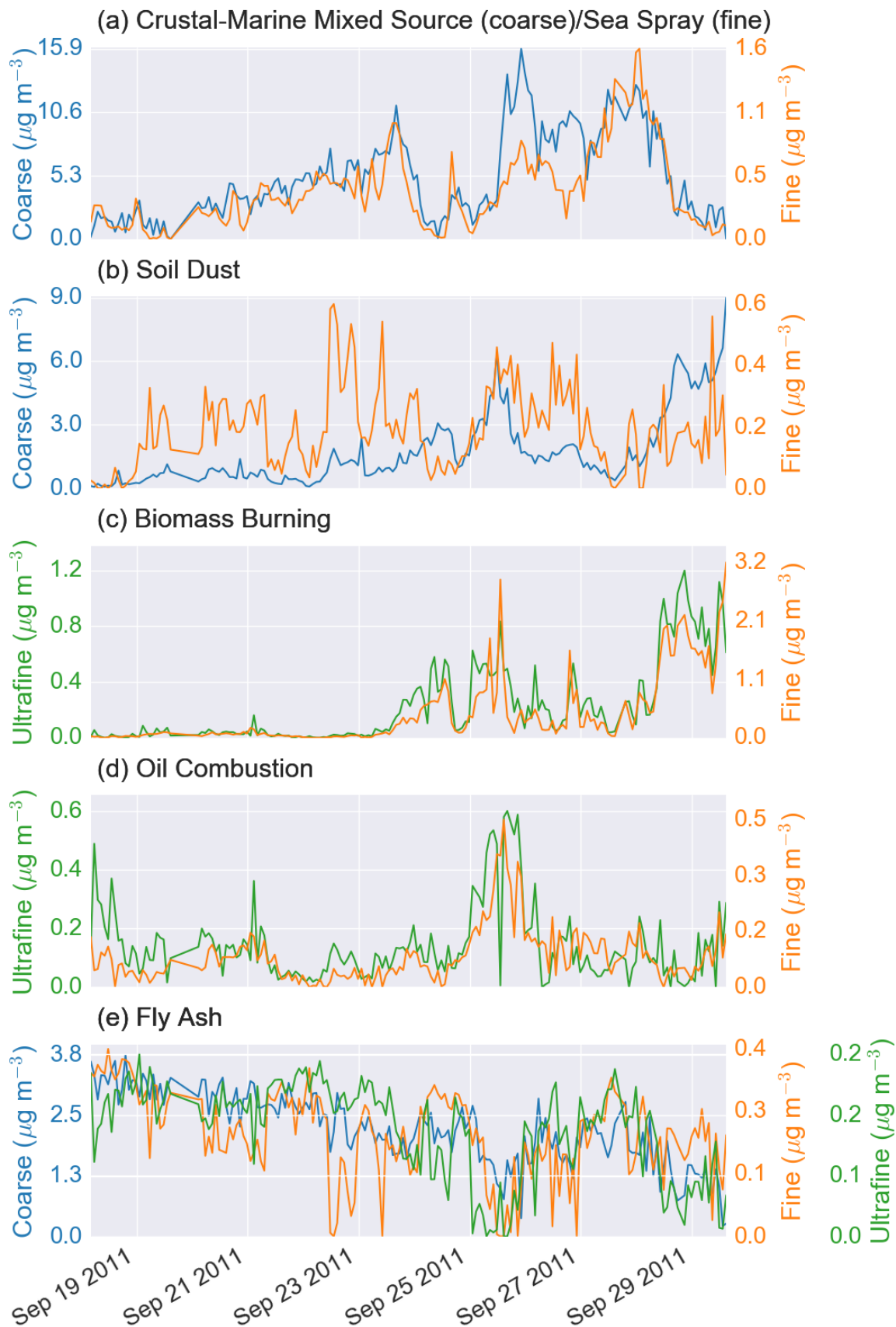
396 **Figure 6. PMF source profiles across different size ranges displayed by percent of species sum for (a) crustal-marine**  
397 **mixed source, (b) soil dust, (c) biomass burning, (d) oil combustion, and (e) fly ash. Coarse: Stage 1-3 (1.15-10  $\mu\text{m}$ ;**  
398 **blue), Fine: Stage 4-6 (0.34-1.15  $\mu\text{m}$ ; orange), Ultrafine: Stage 7-8 (0.10-0.34  $\mu\text{m}$ ; green).**

399 **Crustal-marine mixed source:** The crustal-marine mixed source was resolved in the coarse mode and is characterized  
400 by high apportionments for Mg, Cl, P, Al, Si, S and Ca (Fig. 6a). This source explains nearly half of the variation in crustal  
401 elements such as Al, Si, and Ca. Na and Cl show the highest contribution to the factor mass which indicate marine influence  
402 (Fig. S4, Supplementary material). These elements are indicative of a mix of marine and crustal emissions (Han et al., 2006;  
403 Wang et al., 2014), thus its identification as a crustal-marine mixed source. The mixed nature of the source points to the  
404 covariance of local crustal emissions from islands of the Maritime Continent and those nearby with sea spray. Cl has been  
405 treated as the tracer for this factor due to its high factor sum apportionment (Fig. S4, Supplementary material) and is considered  
406 marine in origin under the assumption that the sampled Cl originated from freshly produced sea spray (Atwood et al., 2013a).  
407 This is likely the case for the cruise as sampling was done over sea water. The factor showed quite high mass contributions to  
408 the coarse mode (56.8%) indicating its dominant influence on coarse elemental PM (Fig.5a). Although both this factor and the  
409 coarse mode soil dust factor are related to crustal emissions, the crustal-marine mixed source is distinct from the coarse mode  
410 soil dust factor in terms of its temporal trend, most apparent during the 28-30 Sept aerosol event (Fig. 7a, b).

411 **Sea Spray:** This factor was resolved in the fine mode and shows high apportionments for Na, Mg, Cl, and Ca. The  
412 identification of the factor as sea spray is evidenced by the nearly 100% source apportionment of Cl. This factor showed fine  
413 (30.4%) modes, attributed to the sampling location over water. As noted above, the appearance of this factor in the PMF  
414 analysis is due to the persistence of Cl in the 0.75-1.15  $\mu\text{m}$  of the DRUM sampler (Fig. 3h). The covariance of the sea spray  
415 factor in the fine mode with the crustal-marine mixed source in the coarse mode point to the influence of marine emissions to  
416 some extent in both the fine and coarse modes, as suggested by a moderate correlation coefficient (0.67) between  $\text{PM}_{10}$  and  
417  $\text{PM}_{2.5}$  Cl (Table 1).

418 **Soil dust:** This factor was characterized by the presence of Fe, Al, Si, K, Ca, Ti, and Zn in the coarse mode and Fe, Cr,  
419 Mn, and Y in the fine mode (Fig. 6b; Table 2). Several of these elements are associated with soil dust (Artaxo et al., 1990,  
420 1998; Lestari et al., 2009; Wimolwattanapun et al., 2010; Gugamsetty et al., 2012). Soil dust may originate from the nearby  
421 island of Palawan but also can potentially come from Borneo. The PMF model was able to distinguish between the crustal-  
422 marine mixed source and soil dust factors. As crustal-marine mixed emissions are assumed to be freshly sampled during the  
423 cruise and the temporal trends of the two sources are distinct (Fig. 7a, b), this suggests the possibility of a long-range transport  
424 mechanism for coarse mode soil dust. The time series of coarse soil dust (Fig. 7b) tracks the fine biomass burning factor well  
425 (Fig. 7c), indicative of coarse soil dust particles entrained in biomass burning plumes. Fe serves as our tracer for soil dust due  
426 to its high apportionment in both soil dust modes. This factor showed mass contributions of 18.7% and 14.0% in the coarse  
427 and fine modes, respectively, which indicates the predominantly coarse mode contribution of the factor (Fig. 5a, b).

428 **Biomass burning:** This factor was characterized by high levels of K and S, and moderate levels of Al, As, and Si which  
429 were found to be associated with biomass burning in previous studies (Artaxo et al., 1998; Han et al., 2006; Lestari et al., 2009;  
430 Atwood et al., 2013a; Alam et al., 2014) (Fig. 6c; Table 2). The factor showed the highest percent contributions to the PM  
431 mass: 32.4% and 45.9% in the fine and ultrafine modes, respectively. The sources of the 26 Sept and 28-30 Sept events (Fig.  
432 7c) will be investigated in Section 5. The presence of crustal elements Fe, Si, and Al in the source profile and the covariance  
433 of the coarse soil dust factor (Fig. 7b) with this factor (Fig. 7c) indicate possible soil dust entrainment during burning updraft  
434 (Reid et al., 2015; Schlosser et al., 2017).



435

436 **Figure 7. Temporal distribution of PMF source contributions ( $\mu\text{g}/\text{m}^3$ ) for (a) crustal-marine mixed source, (b) soil dust,**  
 437 **(c) biomass burning, (d) oil combustion, and (e) fly ash. Coarse: Stage 1-3 (1.15-10  $\mu\text{m}$ ; blue), Fine: Stage 4-6 (0.34-1.15**  
 438  **$\mu\text{m}$ ; orange), Ultrafine: Stage 7-8 (0.10-0.34  $\mu\text{m}$ ; green).**

439 **Oil combustion:** This factor was characterized by high levels of V (Fig. 7d; Table 2), a well-documented tracer for oil  
440 combustion (Hedberg et al., 2005; Mazzei et al., 2008; Becagli et al., 2012). As shown in Fig. 5, the oil combustion factor only  
441 appeared in the fine and ultrafine sizes, contributing 7.3% and 26.1%, respectively, to the total elemental PM mass. The  
442 increasing contribution towards finer stages corroborates the identification of the factor as an anthropogenic source. The  
443 presence of oil combustion is expected as the SCS/WPS hosts high shipping volume, particularly in parts of the Borneo coast  
444 (Fig. S3, Supplementary material).

445 **Fly ash:** This factor was observed in all size modes, characterized by high levels of trace metals Ni, Ga, Zn, Se, Br, Rb,  
446 Pb across modes with slight differences in composition per mode (Fig. 6e); and a source contribution without distinct events  
447 (Fig. 7e). The dominance of Ni, Zn, Se, and Br are indicative of fly ash (Davison et al., 1974; Markowski et al., 1985; Deonarine  
448 et al., 2015). Moderate apportionments of crustal elements Na, Mg, Al, Si, P, and Ti are also observed, suggestive of entrained  
449 soil. The source contribution time series shows a background-type signal. The factor contributed 24.5%, 16.0% and 28.0% to  
450 the total elemental PM mass for the coarse, fine, and ultrafine modes, respectively (Fig. 5). Long-range transport of fly ash  
451 from coal-fired power plants in Indonesia or mainland Malaysia may be responsible for the appearance of the factor as no local  
452 coal-fired power plants could be found upwind of the sampling site in 2011.

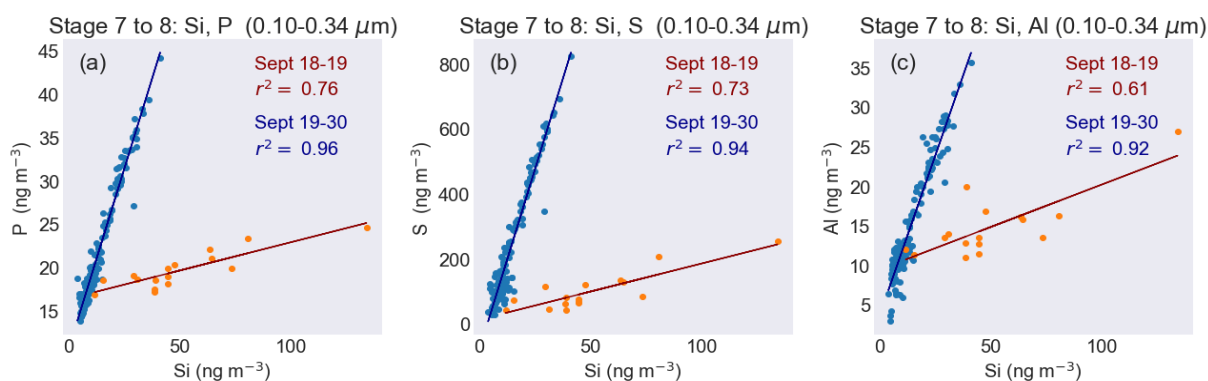
453 The PMF analysis resolved the presence of six sources across the ultrafine, fine and coarse modes which aids in directing  
454 further analysis by identifying key species in the source profiles. Pearson correlation heatmaps (Fig. S5-7, Supplementary  
455 material) and matrices with numerical values (Tables S1-S3, Supplementary material) were constructed to examine the  
456 relationships between species. The first column of the correlation outputs (Fig. S5-7, Tables S1-S3, Supplementary material)  
457 shows the correlation coefficient of the element when compared to the summed elemental PM for that mode. Similar groupings  
458 of elements were observed when compared to the PMF source profiles, indicating the robustness of the analysis. In the coarse  
459 mode (Fig. S5, Table S1, Supplementary material), we observe high correlations between Na, Mg, Cl, P, S, K, Ca, Br, and Sr,  
460 which are associated with sea spray and crustal sources (Han et al., 2006; Wang et al., 2014). Fe, Ti, Mn, Si, and Zn show  
461 moderate to high correlations in the coarse mode, indicative of dust (Karanisiou et al., 2009; Wimolwattanapun et al., 2010;  
462 Lin et al., 2015; Landis et al., 2017). In the fine mode, moderate to high correlations between Al, Si, P, S, K, Br are observed  
463 (Fig. S6, Table S2, Supplementary material). Several of these biomass burning elements show similarly strong correlations in  
464 the ultrafine mode (Fig. S7, Table S3, Supplementary material). V and Ni show a high correlation coefficient (0.91) in the  
465 ultrafine mode, indicative of oil combustion.

466 The excellent correspondence between the observed groupings of elements based on correlation (Tables S2-4,  
467 Supplementary material) and the sources resolved by PMF (Table 2) adds confidence to the identification of key sources during  
468 the cruise. However, as PMF is an unsupervised technique, it may not sufficiently disaggregate significant, consecutive aerosol  
469 events. Visually, two distinct ultrafine events occur between 18 Sept and 19 Sept in Si (Fig. 4b) and V, Ni (Fig. 4d) which are

470 merged by PMF in its oil combustion factor (Fig. 7d). The disproportionate enhancement of ultrafine-mode Si over V and Ni  
471 suggests a source apart from oil combustion. Thus, to further expand on the relationships between elements, we turn to  
472 regression analysis.

#### 473 4.2. Regressions of selected elements

474 An ultrafine Si event between 18 Sept and 19 Sept was shown in the mass size distribution (Fig. 3d) and the time series  
475 (Fig. 4b) of ultrafine Si. Fly ash was the hypothesized source of the ultrafine Si signal; however, although the PMF analysis  
476 suggested the presence of fly ash, ultrafine Si was not significantly apportioned to the fly ash factor (Fig. 6e). Additionally,  
477 none of the factor contributions from PMF showed a similar trend between 18-19 Sept as that of ultrafine Si. This suggests  
478 that PMF may have mishandled the early Si enhancement (Fig. 4b) by merging it with an enhancement in V, Ni that occurred  
479 soon after (Fig. 4d). Regressions show that, between 18 Sept and 19 Sept, Si had distinct ratio slopes and moderate correlations  
480 with P ( $r^2 = 0.76$ ), S ( $r^2 = 0.73$ ), and Al ( $r^2 = 0.61$ ) (Fig. 8; Table S4, Supplementary material) but poor correlations with fly  
481 ash tracers (As, Se, Pb;  $r^2 < 0.12$ ). The high correlations of Si with P, Al, and S suggest a distinct source of Si between 18 Sept  
482 and 19 Sept versus the rest of the cruise; but the low correlations with fly ash tracers rule out fly ash as a possible source. As  
483 the *Vasco* was travelling near islands, the source of the ultrafine Si enhancement is likely a local source en-route to Palawan.  
484 The sudden enhancement may be related to a rapid nucleation event as even submicron dust can be an important source of  
485 CCN in marine/coastal environments (Twohy et al. 2009).



486  
487 **Figure 8. Linear regressions of ultrafine Si and its most highly correlated elements (a) P, (b) S, (c) Al, divided by cruise**  
488 **period before Sept 19 (red) and after Sept 19 (blue).**

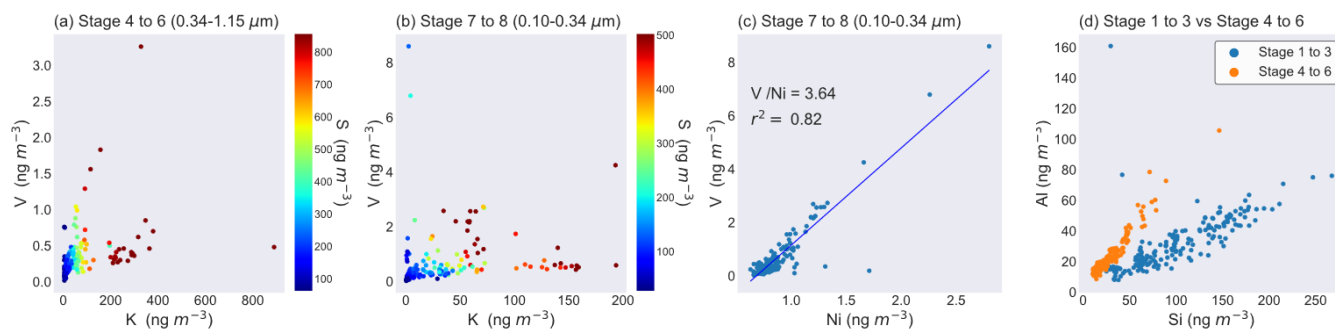
489 As S is an indicator of general combustion (Atwood et al., 2013a), it is important to elucidate its relationship with tracers  
490 of other combustion sources. Multiple linear regression was performed on S on the fine and ultrafine modes (Fig. S8,  
491 Supplementary material). It was found that K and V were excellent predictors of S for most of the cruise but the model required  
492 the addition of Al to capture the variance in S between 24 Sept and 26 Sept, suggesting an additional source during this period  
493 separate from biomass burning or oil combustion. A detailed description of the multiple linear regression analysis can be found  
494 in the Supplementary material. Further examining the relationships of S to these combustion sources, fine and ultrafine mode

495 linear regressions of K and V, colored by the concentration of S per given time, were constructed to show the relationships  
496 between the three species (Fig. 9a, b). S covaries more with K than V as seen with the clearer color gradient along the K-axis,  
497 suggesting the origin of S during the cruise to be more dominantly from biomass burning rather than oil combustion.

498 The ratio between V and Ni is often used as an indicator of the type of oil combustion source (Hedberg et al., 2005;  
499 Nigam et al., 2006; Mazzei et al., 2008; Becagli et al., 2012; Lin et al., 2015). Linear regression plots of V and Ni have a slope  
500 of 3.64 in the ultrafine mode (Fig. 9c). Nigam et al. (2006) measured a V/Ni ratio of 3.5-4 when sampling shipping emissions  
501 directly from the exhausts of various ship engines which suggests shipping to be the main source of ultrafine mode oil  
502 combustion during the cruise.

503 As soil composition varies geographically, soil dust ratios are excellent indicators of a plume's origin (Prospero et al.,  
504 1999; Song et al., 2006; Witt et al., 2006). Figure 8d shows linear regressions of soil dust elements in the coarse and fine  
505 modes. Al and Si, well-known indicators of dust (Viana et al., 2008; Tian et al., 2016; Landis et al., 2017), show moderate  
506 correlations with each other in the coarse and fine modes but slightly differ in ratio-slopes between the fine (Al/Si ~ 1.3;  $r^2 =$   
507 0.94) and coarse (Al/Si ~ 0.93;  $r^2 = 0.78$ ) modes (Fig. 9d). This is indicative of varying sources of fine and coarse mode soil,  
508 with coarse mode soil dust enriched in Si; however, this could also be a matrix effect from the XRF analysis. As the *Vasco*  
509 remained near Palawan island, local dust could be the source of coarse-mode Si-enrichment; however, soil dust from Borneo  
510 is also a possibility.

511 The regression analysis showed an early-cruise enhancement in ultrafine Si that was merged by PMF with a V, Ni  
512 enhancement that occurred soon after, highlighting the importance of the regression analysis in addition to PMF to investigate  
513 the temporal characteristics of sources via elemental tracers. We suggest a local source en-route to the main sampling area to  
514 be the cause of the enhancement but fly ash is unlikely the source due to low correlations with its tracers As, Pb, and Se. The  
515 analysis also showed the strong associations of S with biomass burning and oil combustion; however, S was shown to covary  
516 more significantly with the former. Oil combustion was determined to originate from shipping as indicated by a V/Ni ratio  
517 within the range of that measured by a previous shipping emission study. Finally, we infer multiple sources of soil dust between  
518 the coarse and fine modes due to distinct Si-Al ratios between modes; however, we are unable to determine the exact sources  
519 due to lack of information regarding local and regional soil dust ratios.



520

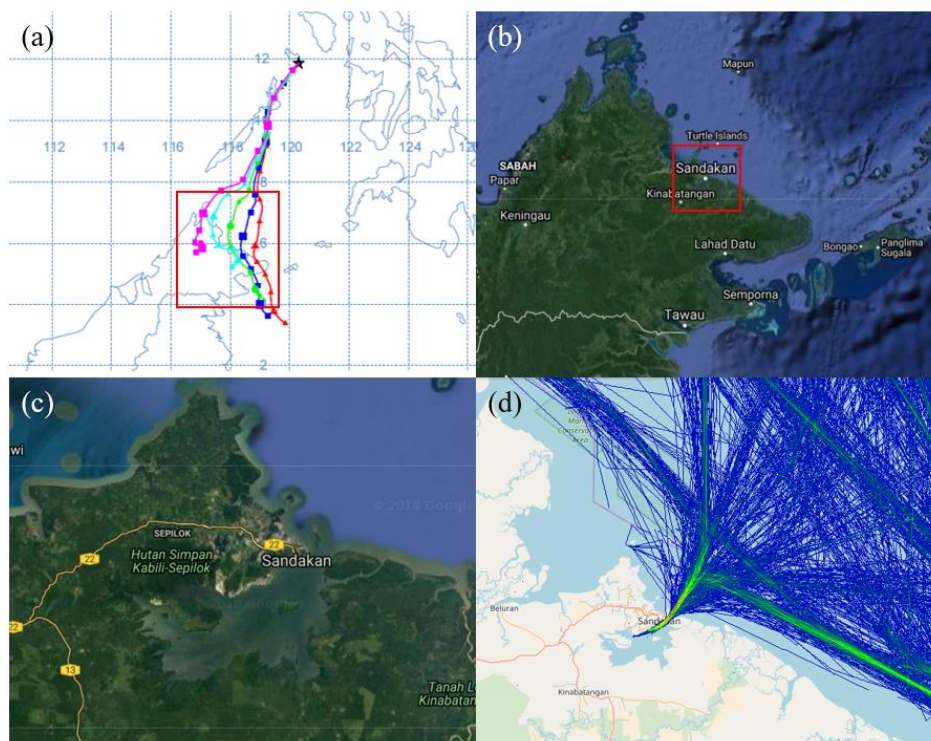
521 **Figure 9. Scatter plot of key species during the cruise. (a) fine mode K, V colored by the concentrations of S at a given**  
522 **time, (b) ultrafine mode K, V likewise colored by concentrations of S at a given time, (c) ultrafine mode V, Ni, and (d)**  
523 **coarse and fine mode Al, Si.**

## 524 **5. Results III: Back trajectory analysis**

### 525 **5.1. 18-19 Sept: Ultrafine V, Ni enhancement from Sandakan, Sabah**

526 As described in Section 3, ultrafine mode V and Ni show a maximum around 18 Sept (Fig. 4d). As the *Vasco* was traveling  
527 near local islands, the event may originate from a local source; however, back trajectories propose an oil combustion source  
528 in Borneo. Back trajectories were generated every hour between 14:00 to 18:00 UTC (corresponding to 22:00 to 02:00 LT) on  
529 18 September and show a westward shift along the eastern coast of Borneo (Fig. 10a). The coast of Borneo is largely forest  
530 (Fig. 10b) but hosts the city of Sandakan, one of Sabah's major ports (Fig. 10c, d). In addition to shipping traffic (Fig. 10d),  
531 Sandakan contains oil depots which are a major source of industry in the area. During the westward shift of the back  
532 trajectories, air masses pass through Sandakan at around 16:00 UTC, approximately the time of the sampled spike in V. The  
533 shipping activity and oil depots present in this area may be responsible for the spike in oil combustion tracers, indicating the  
534 complexity of aerosol transport in the region as small cities like Sandakan may be a source of significant spikes in aerosol.

535



536 **Figure 10. Determination of 18 September event using (a) HYSPLIT back trajectories, (b, c) Google Maps view of the**  
537 **northeastern coast of Borneo (map data ©2018 Google), (d) Density of shipping traffic from Sandakan, Sabah (source:**  
538 **MarineTraffic). Red squares indicate the location of the succeeding plot.**

### 539 **5.2. 20-24 Sept: Clean marine period**



540 The first half of the cruise showed the lowest concentrations of elements associated with biomass burning K, S, Si, and  
541 Al. Back trajectories during this early period originate from the northern part of Borneo and do not penetrate deeply into the  
542 MC until late into the cruise (Fig. 2l). During this period, HYSPLIT back trajectories show that air mass pathways shift away  
543 from the Borneo coasts towards open sea (Fig. 2j). In addition to the shift away from biomass burning sites, back trajectories  
544 between 22 and 24 Sept pass through areas of open sea that host lower levels of shipping traffic (Fig. S3, Supplementary  
545 material).

### 546 **5.3. 24-26 Sept: Large mixed aerosol event from northwest Borneo**

547 Around 26 Sept, increases in fine mode V and Ni occurred when air masses passed through the northwest coast of Borneo,  
548 suggesting the presence of ports or oil depots like with the aforementioned spike on 18 Sept from Sandakan. Back trajectories  
549 generated every 6 hours starting from 24 Sept 15:00 UTC until 26 Sept 09:00 UTC show little change over this period (not  
550 shown) and intersect with the shipping route hub located along northwest Borneo which would explain the V and Ni spikes  
551 (Fig. 2k, S1, Supplementary material). The enrichments of biomass burning and combustion tracers K and S in the sampled  
552 air mass span a wider period beginning on 24 Sept until 26 Sept. This may be due to burning activity along the coast of Borneo  
553 which hosts several MODIS-detected active fire hotspots. Late-night land breeze from the island may have advected polluted  
554 air masses towards the coast.

### 555 **5.4. 28-30 Sept: Large biomass burning event from Southern Kalimantan**

556 Enhancements of these elements after 28 Sept coincide with a regional increase in AOD (Fig. 2d) and are captured by  
557 the NAAPS model in the form of a large smoke event advected northeast (Fig. 2h). Linear regressions show this large aerosol  
558 event at the end of the cruise as a distinct group of points with enhanced concentrations of K and S (Fig. S9, Supplementary  
559 material), suggesting an increase in biomass burning activity during this time. Reid et al. (2015) observed a sharp increase in  
560 the number of active fire hotspots, particularly in Sumatra and Southern Kalimantan. As discussed prior and depicted in Fig.  
561 2, TC Nesat played a major role in synoptic wind patterns during the cruise, causing a shift in back trajectories after 28 Sept  
562 to the southwest coast of Borneo island. Thus, the enhancements of submicron K, S, Si and Al likely originate from biomass  
563 burning in the MC.

## 564 **6. Summary and conclusions**

565 This study describes the size-resolved aerosol elemental composition of particles collected by a DRUM rotating impactor  
566 during the 17 to 30 September 2011 M/Y *Vasco* cruise in the vicinity of the Palawan island of the Philippines. This region was  
567 chosen due to its location as a receptor for MC aerosol sources, such as biomass burning, oil combustion and soil dust.  
568 Meteorological conditions during the cruise were conducive to southwesterly long range transport for seasonal burning aerosol  
569 which was observed in the concentration time series of tracers and satellite-derived AOD. Size-resolved aerosol composition  
570 in the coarse (1.15-10  $\mu\text{m}$ ), fine (0.34- 1.15  $\mu\text{m}$ ) and ultrafine (0.10-0.34  $\mu\text{m}$ ) modes were used as key tracers to ascertain

571 source contributions. Despite the meteorological complexity of the SCS/WPS, we can gain insights into aerosol sources by  
572 focusing on key elemental species. The time series of key elements showed distinct events on 18-19 Sept, 24-26 Sept, and 28-  
573 30 Sept, with clean aerosol periods between events. These aerosol events served as case studies of sources in the region. While  
574 biomass burning is indeed a key source of aerosol, other sources such as oil combustion, crustal-marine mixed source, fly ash,  
575 and soil dust contribute to the chemical profile of the SCS/WPS during the southwest monsoon. Understanding these sources  
576 is key to characterizing aerosol composition and transport in the SCS/WPS and, by extension, developing our understanding  
577 of aerosol-cloud behavior in the region. As back trajectory analysis and aerosol chemistry showed the presence of multiple  
578 key sources, the general conclusions of the study show that:

- 579 1. Mass distributions of key elements showed the evolution of aerosol chemistry throughout the cruise and  
580 interesting covariances between modes. Stage 5 (0.56-0.75  $\mu\text{m}$ ) and stage 7 (0.26-0.34  $\mu\text{m}$ ) showed enhanced  
581 peaks in several elements associated with combustion. Throughout the cruise, mass distributions of V and Ni  
582 track each other well both temporally and across DRUM stages, indicative of oil combustion. Mass distributions  
583 of V and Ni show higher values in the ultrafine mode between 18-19 September, indicative of an early oil  
584 combustion-enriched air mass which was identified to possibly originate from Sandakan, Sabah in Borneo. Mass  
585 distributions of K, Al and S show large enhancements in the fine and ultrafine modes after 27 September,  
586 corroborated by a reported large aerosol event from Reid et al. (2015). The strong peaks of these biomass burning  
587 tracers, in combination with the rapid spread of high AOD and NAAPS-modelled smoke concentration across  
588 the region, provide evidence for intensive emissions from the MC. Coarse-mode soil dust elements such as Fe  
589 and Si showed similarly-timed enhancements, attributed to soil particle entrainment during burning.
- 590 2. Short-term meteorological events such as the tropical cyclone (TC) Nesat played a key role in long-range  
591 transport as they propagated through the region, expediting the northeastward advection of aerosol emissions, an  
592 effect observed in previous studies (Atwood et al., 2013a; Reid et al., 2012, 2015). The sudden variations in  
593 aerosol concentration after 24 Sept can be connected to the movement of TC Nesat through the region. Prior to  
594 these events, aerosol concentrations remained at generally low levels as NAAPS shows smoke was largely  
595 constrained to the southern hemisphere. The passage of TC Nesat advected air masses more northward, allowing  
596 them to penetrate deep enough into the northern hemisphere to be sampled by the *Vasco*. The TC's passage  
597 coincided with a shift in air mass origin from mainland Malaysia prior to 24 Sept to areas known for intense  
598 burning activity, most notably Southern Kalimantan by the end of the cruise. This corresponded to a mixed  
599 aerosol event from 24 to 26 Sept attributed to Brunei, Borneo and a significant increase in biomass burning tracer  
600 concentrations from 28 to 30 Sept attributed to Southern Kalimantan. Between these aerosol events, a clean  
601 marine event from 26 until 28 Sept was characterized by high concentrations of Cl and low levels of elements  
602 associated with anthropogenic sources. Back trajectories showed that air masses travelled through the open,

603 central SCS/WPS which suggest a good signal of sea spray was sampled. As the ship route brought the *Vasco*  
604 near islands, local crustal emissions covaried with sea spray aerosol which resulted in the crustal-marine mixed  
605 source during the PMF analysis.

- 606 3. Six sources across the three size modes were resolved by the PMF analysis: biomass burning, oil combustion,  
607 soil dust, crustal-marine mixed source, sea spray, and fly ash. A threshold Pearson R coefficient of 0.0 was used  
608 to filter species included in the PMF analysis to improve the interpretability of the PMF solution. Results show  
609 that natural sources – the crustal-marine mixed source and soil dust factors - were observed in only the coarse  
610 and fine modes while anthropogenic sources, biomass burning, oil combustion, and fly ash, were resolved purely  
611 in the fine and ultrafine modes. A strong correspondence between key elements seen on the PMF source profiles  
612 and groupings of these elements on the correlation matrices adds confidence to the PMF solution. The biomass  
613 burning PMF factor showed the highest percent contributions to total elemental PM mass in the fine and ultrafine  
614 modes: 32.4% in the fine mode, and 45.9% in the ultrafine mode. It is interesting to note that the relative  
615 contribution of the oil combustion factor increased significantly towards finer modes, 7.3% in the fine mode but  
616 26.1% in the ultrafine mode, corroborating its anthropogenic identification. In terms of aerosol events, PMF  
617 source contributions were able to capture the most events seen in the raw elemental concentrations. Differences  
618 in the temporal variations between PMF-resolved sources suggest these sources are distinct. However, PMF did  
619 not differentiate between an early ultrafine Si spike from a distinct, subsequent spike in V which demonstrates  
620 that PMF may merge events, leading to a loss in resolution as observed in other studies (Van Pinxteren et al.,  
621 2016). This, however, can be ameliorated with an in-depth, supervised analysis of the data as done in this study.
- 622 4. As stated above, spikes in oil combustion tracers V and Ni were observed on 18 Sept in the fine and ultrafine  
623 modes. HYSPLIT back trajectories suggest the origin of the air mass as Sandakan, an industrial area and port  
624 city of Sabah known for its oil depots and shipping activity located along the northeastern coast of Borneo. The  
625 spike in oil combustion suggest that a small city can cause drastic increases in tracer concentration depending on  
626 air mass trajectories. The strong presence of ultrafine mode Si from 18-19 September was also observed but the  
627 time series of Si is distinct from the time series of V and Ni, suggestive of a source distinct from oil combustion.
- 628 5. The 24 to 26 September event coincided with the arrival of TC Nesat east of Luzon (northeast of the *Vasco*'s  
629 location). Enhancements of multiple key tracers for biomass burning, oil combustion and soil dust were observed,  
630 indicative of aerosols mixing within an air mass during transport. Biomass burning tracers K, S, Si, Al show  
631 enhancements over a wider period (24-26 Sept) than that of oil combustion tracers V and Ni, which spiked at the  
632 end of the period. Furthermore, aerosol-convection interactions were observed as sharp dips in the concentrations  
633 of biomass burning and soil dust tracers around 25 Sept before recovery. Interestingly, this dip was not observed  
634 for oil combustion tracers V, Ni. This cold pool event was reported in detail by Reid et al. (2015) and this study

635 further elaborated on its impact on PM of different elemental composition. This case demonstrates the effect of  
636 short-term or high frequency phenomena on aerosol transport in the MC. HYSPLIT back trajectories show that  
637 air masses begin to travel from the southwest MC in response to TC Nesat's inflow arm. Air masses during the  
638 24-26 September event pass through Brunei, a shipping hub located along the northeastern coast of Borneo,  
639 which explains the increase in oil combustion tracers V and Ni. The coast was also observed to host a number of  
640 active fire hotspots. Land breeze may lead to the entrainment of burning plumes into the traveling air mass which  
641 would explain the enrichment.

- 642 6. The 28-30 September aerosol event showed an enrichment in K and S that coincided with a shift in back trajectory  
643 origin to Southern Kalimantan, which hosts a high fire hotspot density. MC burning may be characterized by an  
644 elevated K/S ratio and strong fine and ultrafine mode peaks in the mass distributions of S and K. The 28-30  
645 September event also coincided with the enhancement of soil dust elements in the coarse mode, indicative of soil  
646 particle entrainment during burning activity (Reid et al., 2015).

647 The study identified source locations of aerosol and characterized the plumes during the *Vasco* 2011 cruise; however,  
648 unanswered questions remain such as the origin of the strong ultrafine Si signal detected early in the cruise (18-19 Sept) which  
649 may be connected to a rapid local nucleation event. The source location of the PMF-resolved fly ash factor also remains  
650 unidentified due to its complicated source contribution time series and unclear elemental profile. Investigation into cloud nuclei  
651 (CN) properties during the cruise may be done to further validate the intensity and timing of plumes. In addition to the findings  
652 of this study on the elemental PM, future research on other species collected during the 2011 and 2012 *Vasco* campaigns such  
653 as trace gases may compliment and deepen our current understanding of the aerosol environment in the SCS/WPS through  
654 additional degrees of freedom, specifically utilizing the lifetimes of trace gases and inferring the potential for secondary aerosol  
655 formation during transport.

#### 656 **Author contribution**

657 MRAH performed the analysis and prepared the manuscript. MTC supervised the analysis, especially for the PMF  
658 section. MOLC supervised the analysis and provided input for the manuscript. JSR collected the data onboard the *Vasco*,  
659 supervised the analysis, provided input for the manuscript. PX provided the NAAPS Smoke model outputs for Fig. 2 and  
660 provided input for the manuscript. JBS, NDL, SNYU collected the data onboard the *Vasco*. SC, YJZ performed the XRF  
661 analysis on the data.

#### 662 **Data availability**

663 The *Vasco* ship data is available through correspondence with Jeffrey S. Reid, jeffrey.reid@nrlmry.navy.mil. MODIS  
664 AOD images were obtained from the NASA Worldview application: <https://worldview.earthdata.nasa.gov/>. HYSPLIT data is

665 accessible through the NOAA READY website (<http://www.ready.noaa.gov>). NAAPS aerosol reanalysis data can be accessed  
666 at the US GODAE server: <http://www.usgoda.gov/>.

## 667 **Competing Interests**

668 The authors declare that they have no conflict of interest.

## 669 **Acknowledgements**

670 We acknowledge the use of imagery from the NASA Worldview application (<https://worldview.earthdata.nasa.gov/>),  
671 part of the NASA Earth Observing System Data and Information System (EOSDIS). The authors gratefully acknowledge the  
672 NOAA Air Resources Laboratory (ARL) for the provision of the HYSPLIT transport and dispersion model and/or READY  
673 website (<http://www.ready.noaa.gov>) used in this publication.

## 674 **References**

- 675 Alam, K., Mukhtar, A., Shahid, I., Blaschke, T., Majid, H., Rahman, S., Khan, R. and Rahman, N.: Source apportionment  
676 and characterization of particulate matter (PM<sub>10</sub>) in urban environment of Lahore, *Aerosol Air Qual. Res.*, 14(7), 1851–  
677 1861, doi:10.4209/aaqr.2014.01.0005, 2014.
- 678 Artaxo, P. and Maenhaut, W.: Aerosol Characteristics and Sources for the Amazon Basin During the Wet Season, *J.*  
679 *Geophys. Res.*, 95(D10), 16971–16985, 1990.
- 680 Artaxo, P., Fernandes, E. T., Martins, J. V., Yamasoe, M. A., Maenhaut, W., Longo, K. M., Castanho, A. and Hobbs, P. V.:  
681 Large-scale aerosol source apportionment in Amazonia, *J. Geophys. Res. Atmos.*, 103(D24), 31837–31847,  
682 doi:10.1029/98jd02346, 1998.
- 683 Atwood, S. A., Reid, J. S., Kreidenweis, S. M., Cliff, S. S., Zhao, Y., Lin, N.-H., Tsay, S.-C., Chu, Y.-C. and Westphal, D.  
684 L.: Size resolved measurements of springtime aerosol particles over the northern South China Sea, *Atmospheric*  
685 *Environment*, 78, 134–143, doi:10.1016/j.atmosenv.2012.11.024, 2013a.
- 686 Atwood, S. A., Salinas, S. V., Chew, B. N., Reid, J. S., Balasubramanian, R., Yu, L. E. and Kreidenweis, S. M.: Analysis of  
687 source regions for smoke events in Singapore for the 2009 El Nino burning season, *Atmos. Environ.*, 78, 219–230,  
688 doi:10.1016/j.atmosenv.2013.04.047, 2013b.
- 689 Atwood, S. A., Reid, J. S., Kreidenweis, S. M., Blake, D. R., Jonsson, H. H., Lagrosas, N. D., Xian, P., Reid, E. A., Sessions,  
690 W. R. and Simpas, J. B.: Size-resolved aerosol and cloud condensation nuclei (CCN) properties in the remote marine  
691 South China Sea-Part 1: Observations and source classification, *Atmos. Chem. Phys.*, 17(2), 1105–1123,  
692 doi:10.5194/acp-17-1105-2017, 2017.

693 Baker, K. R., Simon, H. and Kelly, J. T.: Challenges to modeling “cold pool” meteorology associated with high pollution  
694 episodes, *Environ. Sci. Technol.*, 45(17), 7118–7119, doi:10.1021/es202705v, 2011.

695 Balasubramanian, R., Qian, W.-B., Decesari, S., Facchini, M. C. and Fuzzi, S.: Comprehensive characterization of PM 2.5  
696 aerosols in Singapore, *J. Geophys. Res.*, 108(D16), doi:10.1029/2002jd002517, 2003.

697 Becagli, S., Sferlazzo, D. M., Pace, G., Di Sarra, A., Bommarito, C., Calzolari, G., Ghedini, C., Lucarelli, F., Meloni, D.,  
698 Monteleone, F., Severi, M., Traversi, R. and Udisti, R.: Evidence for heavy fuel oil combustion aerosols from chemical  
699 analyses at the island of Lampedusa: A possible large role of ships emissions in the Mediterranean, *Atmos. Chem. Phys.*,  
700 12(7), 3479–3492, doi:10.5194/acp-12-3479-2012, 2012.

701 Boucher, O., D. Randall, P. Artaxo, C. Bretherton, G. Feingold, P. Forster, V.-M. Kerminen, Y. Kondo, H. Liao, U.  
702 Lohmann, P. Rasch, S.K. Satheesh, S. Sherwood, B. Stevens and X.Y. Zhang: Clouds and Aerosols. In: *Climate Change*  
703 2013: The Physical Science Basis. Contribution of Working Group I to the Fifth Assessment Report of the  
704 Intergovernmental Panel on Climate Change [Stocker, T.F., D. Qin, G.-K. Plattner, M. Tignor, S.K. Allen, J. Boschung,  
705 A. Nauels, Y. Xia, V. Bex and P.M. Midgley (eds.)]. Cambridge University Press, Cambridge, United Kingdom and New  
706 York, NY, USA, 2013.

707 Cahill, T. A., Barnes, D. E., Lawton, J. A., Miller, R., Spada, N., C, R. D. W. and Kimbrough, S.: Transition metals in  
708 coarse, fine, very fine and ultra-fine particles from an interstate highway transect near Detroit, , doi:10.1016/S0065-  
709 3454(07)37008-3, 2007.

710 Chan, Y. C., Christensen, E., Golding, G., King, G., Gore, W., Cohen, D. D., Stelcer, E., Simpson, R., Denison, L. and  
711 Wong, N.: Source Apportionment of Ambient Volatile Organic Compounds in Major Cities in Australia By Positive  
712 Matrix Factorisation , 42(2), 22–29, 2008.

713 Chang, C. P., Zhuo, W., John, M. and Ching-Hwang, L.: Annual Cycle of Southeast Asia — Maritime Continent Rainfall  
714 and the Asymmetric, *J. Clim.*, 18, 287–301, doi:10.1175/JCLI-3257.1, 2005.

715 Chow, J. C., Lowenthal, D. H., Chen, L.-W. A., Wang, X. and Watson, J. G.: Mass reconstruction methods for PM2.5: a  
716 review, *Air Qual Atmos Health*, 8(3), 243–263, doi:10.1007/s11869-015-0338-3, 2015.

717 Cohen, D. D., Crawford, J., Stelcer, E. and Bac, V. T.: Long range transport of fine particle windblown soils and coal fired  
718 power station emissions into Hanoi between 2001 to 2008, *Atmos. Environ.*, 44(31), 3761–3769,  
719 doi:10.1016/j.atmosenv.2010.06.047, 2010a.

720 Cohen, D. D., Crawford, J., Stelcer, E. and Bac, V. T.: Characterisation and source apportionment of fine particulate sources  
721 at Hanoi from 2001 to 2008, *Atmos. Environ.*, 44(3), 320–328, doi:10.1016/j.atmosenv.2009.10.037, 2010b.

722 Davison, R. L., Natusch, D. F. S. and Wallace, J. R.: Trace Elements in Fly Ash, , 8(13) [online] Available from:  
723 <https://pubs.acs.org/doi/pdf/10.1021/es60098a003?src=recsys>, 1974.

724 Deonarine, A., Kolker, A. and Doughten, M.: Trace Elements in Coal Ash, *Usgs*, (May), 1–6,  
725 doi:10.1002/9781119199090.fmatter, 2015.

726 Draxler, R. R. and Hess, G. D.: An overview of the HYSPLIT\_4 modelling system for trajectories, *Aust. Meteorol. Mag.*,  
727 47, 295–308, 1998.

728 Draxler, R. R.: HYSPLIT4 user's guide. NOAA Tech. Memo. ERL ARL-230, NOAA Air Resources Laboratory, Silver  
729 Spring, MD., 1999.

730 Duncan, B. N., Martin, R. V., Staudt, A. C., Yevich, R. and Logan, J. A.: Interannual and seasonal variability of biomass  
731 burning emissions constrained by satellite observations, *J. Geophys. Res.*, 108(D2), doi:10.1029/2002jd002378, 2003.

732 Engling, G., He, J., Betha, R. and Balasubramanian, R.: Assessing the regional impact of Indonesian biomass burning  
733 emissions based on organic molecular tracers and chemical mass balance modeling, *Atmos. Chem. Phys.*, 14(15), 8043–  
734 8054, doi:10.5194/acp-14-8043-2014, 2014.

735 Farao, C., Canepari, S., Perrino, C. and Harrison, R. M.: Sources of PM in an industrial area: Comparison between receptor  
736 model results and semiempirical calculations of source contributions, *Aerosol Air Qual. Res.*, 14(6), 1558–1572,  
737 doi:10.4209/aaqr.2013.08.0281, 2014.

738 Field, R. D. and Shen, S. S. P.: Predictability of carbon emissions from biomass burning in Indonesia from 1997 to 2006, *J.*  
739 *Geophys. Res. Biogeosciences*, 113(4), 1–17, doi:10.1029/2008JG000694, 2008.

740 Fujii, Y., Tohno, S., Amil, N., Latif, M. T., Oda, M., Matsumoto, J. and Mizohata, A.: Annual variations of carbonaceous  
741 PM<sub>2.5</sub> in Malaysia: Influence by Indonesian peatland fires, *Atmos. Chem. Phys. Discuss.*, 15(16), 22419–22449,  
742 doi:10.5194/acpd-15-22419-2015, 2015.

743 Ge, C., Wang, J. and Reid, J. S.: Mesoscale modeling of smoke transport over the Southeast Asian maritime continent:  
744 Coupling of smoke direct radiative effect below and above the low-level clouds, *Atmos. Chem. Phys.*, 14(1), 159–174,  
745 doi:10.5194/acp-14-159-2014, 2014.

746 Gugamsetty, B., Wei, H., Liu, C. N., Awasthi, A., Tsai, C. J., Roam, G. D., Wu, Y. C. and Chen, C. F.: Source  
747 Characterization and Apportionment of PM<sub>10</sub>, PM<sub>2.5</sub> and PM<sub>0.1</sub> by Using Positive Matrix Factorization, *Aerosol Air*  
748 *Qual. Res.*, 12(4), 476–491, doi:10.4209/aaqr.2012.04.0084, 2012.

749 Han, J. S., Moon, K. J., Lee, S. J., Ryu, S. Y., Cliff, S. S., Kim, Y. J. and Yi, S. M.: Size-resolved source apportionment of  
750 ambient particles by positive matrix factorization at Gosan background site in East Asia, *Atmos. Chem. Phys.*, 6(1), 211–  
751 223, doi:10.5194/acp-6-211-2006, 2006.

752 Hedberg, E., Gidhagen, L. and Johansson, C.: Source contributions to PM<sub>10</sub> and arsenic concentrations in Central Chile  
753 using positive matrix factorization, *Atmos. Environ.*, 39(3), 549–561, doi:10.1016/j.atmosenv.2004.11.001, 2005.

754 Higgins, R. W. and Shi, W.: Intercomparison of the principal modes of interannual and intraseasonal variability of the North  
755 American Monsoon System, *J. Clim.*, 14(3), 403–417, doi:10.1175/1520-0442(2001)014<0403:IOTPMO>2.0.CO;2,  
756 2001.

757 Hoek, G., Krishnan, R. M., Beelen, R., Peters, A., Ostro, B., Brunekreef, B. and Kaufman, J. D.: Long-term air pollution  
758 exposure and cardio-respiratory mortality: A review, *Environ. Heal. A Glob. Access Sci. Source*, 12(1),  
759 doi:10.1186/1476-069X-12-43, 2013.

760 Hsu, S. C., Tsai, F., Lin, F. J., Chen, W. N., Shiah, F. K., Huang, J. C., Chan, C. Y., Chen, C. C., Liu, T. H., Chen, H. Y.,  
761 Tseng, C. M., Hung, G. W., Huang, C. H., Lin, S. H. and Huang, Y. T.: A super Asian dust storm over the East and South  
762 China Seas: Disproportionate dust deposition, *J. Geophys. Res. Atmos.*, 118(13), 7169–7181, doi:10.1002/jgrd.50405,  
763 2013.

764 Hyer, E. J., Reid, J. S. and Zhang, J.: An over-land aerosol optical depth data set for data assimilation by filtering, correction,  
765 and aggregation of MODIS Collection 5 optical depth retrievals, *Atmos. Meas. Tech.*, 4(3), 379–408, doi:10.5194/amt-4-  
766 379-2011, 2011.

767 Karanasiou, A. A., Siskos, P. A. and Eleftheriadis, K.: Assessment of source apportionment by Positive Matrix Factorization  
768 analysis on fine and coarse urban aerosol size fractions, *Atmos. Environ.*, 43(21), 3385–3395,  
769 doi:10.1016/j.atmosenv.2009.03.051, 2009.

770 Kecorius, S., Madueno, L., Vallar, E., Alas, H., Betito, G., Birmili, W., Cambaliza, M. O., Catipay, G., Gonzaga-Cayetano,  
771 M., Galvez, M. C., Lorenzo, G., Müller, T., Simpas, J. B., Tamayo, E. G. and Wiedensohler, A.: Aerosol particle mixing  
772 state, refractory particle number size distributions and emission factors in a polluted urban environment: Case study of  
773 Metro Manila, Philippines, *Atmos. Environ.*, 170, 169–183, doi:10.1016/j.atmosenv.2017.09.037, 2017.

774 Landis, M. S., Pancras, J. P., Graney, J. R., White, E. M., Edgerton, E. S., Legge, A. and Percy, K. E.: Source apportionment  
775 of ambient fine and coarse particulate matter at the Fort McKay community site, in the Athabasca Oil Sands Region,  
776 Alberta, Canada, *Sci. Total Environ.*, 584–585, 105–117, doi:10.1016/j.scitotenv.2017.01.110, 2017.



- 777 Lareau, N. P., Crosman, E., Whiteman, C. D., Horel, J. D., Hoch, S. W., Brown, W. O. J. and Horst, T. W.: The persistent  
778 cold-air pool study, *Bull. Am. Meteorol. Soc.*, 94(1), 51–63, doi:10.1175/BAMS-D-11-00255.1, 2013.
- 779 Lee, E., Chan, C. K. and Paatero, P.: Application of positive matrix factorization in source apportionment of particulate  
780 pollutants in Hong Kong, *Atmos. Environ.*, 33(19), 3201–3212, doi:10.1016/S1352-2310(99)00113-2, 1999.
- 781 Lee, S.-S., Feingold, G. and Chuang, P. Y.: Effect of Aerosol on Cloud–Environment Interactions in Trade Cumulus, *J.*  
782 *Atmos. Sci.*, 69(12), 3607–3632, doi:10.1175/jas-d-12-026.1, 2012.
- 783 Lestari, P. and Mauliadi, Y. D.: Source apportionment of particulate matter at urban mixed site in Indonesia using PMF,  
784 *Atmos. Environ.*, 43(10), 1760–1770, doi:10.1016/j.atmosenv.2008.12.044, 2009.
- 785 Li, T., Wang, Y., Li, W. J., Chen, J. M., Wang, T. and Wang, W. X.: Concentrations and solubility of trace elements in fine  
786 particles at a mountain site, southern China: Regional sources and cloud processing, *Atmos. Chem. Phys.*, 15(15), 8987–  
787 9002, doi:10.5194/acp-15-8987-2015, 2015.
- 788 Liao, H.-T., Chou, C. C.-K., Chow, J. C., Watson, J. G., Hopke, P. K. and Wu, C.-F.: Source and risk apportionment of  
789 selected VOCs and PM<sub>2.5</sub> species using partially constrained receptor models with multiple time resolution data,  
790 *Environ. Pollut.*, 205, 121–130, doi:10.1016/j.envpol.2015.05.035, 2015.
- 791 Liao, H.-T., Chang, J.-C., Tsai, T.-T., Tsai, S.-W., Chou, C. C.-K. and Wu, C.-F.: Vertical distribution of source apportioned  
792 PM<sub>2.5</sub> using particulate-bound elements and polycyclic aromatic hydrocarbons in an urban area, *J Expo Sci Environ*  
793 *Epidemiol*, 1–11, doi:10.1038/s41370-019-0153-2, 2019.
- 794 Lin, C.-Y., Wang, Z., Chen, W.-N., Chang, S.-Y., Chou, C. C. K., Sugimoto, N. and Zhao, X.: Long-range transport of Asian  
795 dust and air pollutants to Taiwan: observed evidence and model simulation, *Atmos. Chem. Phys. Discuss.*, 6(5), 10183–  
796 10216, doi:10.5194/acpd-6-10183-2006, 2007.
- 797 Lin, Y.-C., Tsai, C.-J., Wu, Y.-C., Zhang, R., Chi, K.-H., Huang, Y.-T., Lin, S.-H. and Hsu, S.-C.: Characteristics of trace  
798 metals in traffic-derived particles in Hsuehshan Tunnel, Taiwan: size distribution, potential source, and fingerprinting  
799 metal ratio, *Atmos. Chem. Phys.*, 15(8), 4117–4130, doi:10.5194/acp-15-4117-2015, 2015.
- 800 Loo, Y. Y., Billa, L. and Singh, A.: Effect of climate change on seasonal monsoon in Asia and its impact on the variability of  
801 monsoon rainfall in Southeast Asia, *Geosci. Front.*, 6(6), 817–823, doi:10.1016/j.gsf.2014.02.009, 2015.
- 802 Lynch, P., Reid, J. S., Westphal, D. L., Zhang, J., Hogan, T. F., Hyer, E. J., Curtis, C. A., Hegg, D. A., Shi, Y., Campbell, J.  
803 R., Rubin, J. I., Sessions, W. R., Turk, F. J. and Walker, A. L.: An 11-year global gridded aerosol optical thickness  
804 reanalysis (v1.0) for atmospheric and climate sciences, *Geosci. Model Dev.*, 9(4), 1489–1522, doi:10.5194/gmd-9-1489-  
805 2016, 2016.

806 Ma, L., Dadashazar, H., Braun, R. A., MacDonald, A. B., Aghdam, M. A., Maudlin, L. C. and Sorooshian, A.: Size-resolved  
807 characteristics of water-soluble particulate elements in a coastal area: Source identification, influence of wildfires, and  
808 diurnal variability, *Atmospheric Environment*, 206, 72–84, doi:10.1016/j.atmosenv.2019.02.045, 2019.

809 Malm, W. C. and Hand, J. L.: An examination of the physical and optical properties of aerosols collected in the IMPROVE  
810 program, *Atmospheric Environment*, 41(16), 3407–3427, doi:10.1016/j.atmosenv.2006.12.012, 2007.

811 Maloney, E. D. and Hartmann, D. L.: The Madden–Julian Oscillation, Barotropic Dynamics, and North Pacific Tropical  
812 Cyclone Formation. Part I: Observations, *J. Atmos. Sci.*, 58(17), 2545–2558, doi:10.1175/1520-  
813 0469(2001)058<2545:TMJOB>2.0.CO;2, 2001.

814 Mazzei, F., D’Alessandro, A., Lucarelli, F., Nava, S., Prati, P., Valli, G. and Vecchi, R.: Characterization of particulate  
815 matter sources in an urban environment, *Sci. Total Environ.*, 401(1–3), 81–89, doi:10.1016/j.scitotenv.2008.03.008,  
816 2008.

817 Markowski, G. R. and Filby, R.: Trace Element Concentration as a Function of Particle Size in Fly Ash from a Pulverized  
818 Coal Utility Boiler, *Environ. Sci. Technol.*, 19(9), 796–804, doi:10.1021/es00139a005, 1985.

819 Nakajima, T., Yoon, S. C., Ramanathan, V., Shi, G. Y., Takemura, T., Higurashi, A., Takamura, T., Aoki, K., Sohn, B. J.,  
820 Kim, S. W., Tsuruta, H., Sugimoto, N., Shimizu, A., Tanimoto, H., Sawa, Y., Lin, N. H., Lee, C. Te, Goto, D. and  
821 Schutgens, N.: Overview of the Atmospheric Brown Cloud East Asian Regional Experiment 2005 and a study of the  
822 aerosol direct radiative forcing in east Asia, *J. Geophys. Res. Atmos.*, 112(24), 1–23, doi:10.1029/2007JD009009, 2007.

823 Nigam, A., Welch, W., Wayne Miller, J., and Cocher III, D. R.: Effect of fuel sulphur content and control technology on PM  
824 emission from ship’s auxiliary engine. Proceeding international aerosol conference, St. Paul, USA, 10–15 September  
825 2006, 1531–1532, 2006.

826 Oanh, Nguyen Thi Kim. *Integrated air quality management: Asian case studies*. Boca Raton, FL: Taylor & Francis, 2013.  
827 Print.

828 O’Sullivan, D. Murray, B. J., Malkin, T. L., Whale, T. F., Umo, N. S., Atkinson, J. D., Price, H. C., Baustian, K. J., Browse,  
829 J. and Webb, M. E.: Ice nucleation by fertile soil dusts: relative importance of mineral and biogenic components, *Atmos.*  
830 *Chem. Phys.*, 14(4), 1853–1867, doi:10.5194/acp-14-1853-2014, 2014.

831 Paatero, P. and Tapper, U.: Positive matrix factorization: A non-negative factor model with optimal utilization of error  
832 estimates of data values, *Environmetrics*, 5(2), 111–126, doi:10.1002/env.3170050203, 1994.

833 Paatero, P. and Hopke, P. K.: Discarding or downweighting high-noise variables in factor analytic models, *Anal. Chim.*  
834 *Acta*, 490(1–2), 277–289, doi:10.1016/S0003-2670(02)01643-4, 2003.

- 835 Paterson, K. G., Sagady, J. L., Hooper, D. L., Bertman, S. B., Carroll, M. A. and Shepson, P. B.: Analysis of air quality data  
836 using positive matrix factorization, *Environ. Sci. Technol.*, 33(4), 635–641, doi:10.1021/es980605j, 1999.
- 837 Polissar, A. V., Hopke, P. K., Paatero, P., Malm, W. C. and Sisler, J. F.: Atmospheric aerosol over Alaska 2. Elemental  
838 composition and sources, *J. Geophys. Res. Atmos.*, 103(D15), 19045–19057, doi:10.1029/98JD01212, 1998.
- 839 Prospero, J. M.: Long-range transport of mineral dust in the global atmosphere: Impact of African dust on the environment  
840 of the southeastern United States, *Proc. Natl. Acad. Sci.*, 96(7), 3396–3403, doi:10.1073/pnas.96.7.3396, 1999.
- 841 Qi, L., Chen, M., Ge, X., Zhang, Y. and Guo, B.: Seasonal variations and sources of 17 aerosol metal elements in suburban  
842 Nanjing, China, *Atmosphere (Basel)*, 7(12), 1–21, doi:10.3390/atmos7120153, 2016.
- 843 Qian, J.-H., Robertson, A. W. and Moron, V.: Interactions among ENSO, the Monsoon, and Diurnal Cycle in Rainfall  
844 Variability over Java, Indonesia, *J. Atmos. Sci.*, 67(11), 3509–3524, doi:10.1175/2010jas3348.1, 2010.
- 845 Querol, X., Viana, M., Alastuey, A., Amato, F., Moreno, T., Castillo, S., Pey, J., Rosa, J. de la, Campa, A. S. de la, Artinano,  
846 B., Salvador, P., Santos, S. G. Dos, Fernandez-Patier, R., Moreno-Grau, S., Negral, L., Minguillon, M. C., Monfort, E.,  
847 Gil, J. I., Inza, A., Ortega, L. A., Santamaria, J. M. and Zabalza, J.: Source origin of trace elements in PM from regional  
848 background, urban and industrial sites of Spain, *Atmos. Environ.*, 41(34), 7219–7231,  
849 doi:10.1016/j.atmosenv.2007.05.022, 2007.
- 850 Raabe, O. G., Braaten, D. A., Axelbaum, R. L., Teague, S. V and Cahill, T. A.: Calibration studies of the drum impactor, *J.*  
851 *Aerosol Sci.*, 19(2), 183–195, doi:10.1016/0021-8502(88)90222-4, 1988.
- 852 Reid, J. S., Flocchini, R. G., Cahill, T. A., Ruth, R. S. and Salgado, D. P.: Local meteorological, transport, and source  
853 aerosol characteristics of late autumn Owens Lake (dry) dust storms, *Atmos. Environ.*, 28(9), 1699–1706,  
854 doi:10.1016/1352-2310(94)90315-8, 1994.
- 855 Reid, J. S., Hyer, E. J., Prins, E. M., Westphal, D. L., Zhang, J., Wang, J., Christopher, S. A., Curtis, C. A., Schmidt, C. C.,  
856 Eleuterio, D. P., Richardson, K. A. and Hoffman, J. P.: Global monitoring and forecasting of biomass-burning smoke:  
857 Description of and lessons from the fire Locating and Modeling of Burning Emissions (FLAMBE) program, *IEEE J. Sel.*  
858 *Top. Appl. Earth Obs. Remote Sens.*, 2(3), 144–162, doi:10.1109/JSTARS.2009.2027443, 2009.
- 859 Reid, J. S., Xian, P., Hyer, E. J., Flatau, M. K., Ramirez, E. M., Turk, F. J., Sampson, C. R., Zhang, C., Fukada, E. M. and  
860 Maloney, E. D.: Multi-scale meteorological conceptual analysis of observed active fire hotspot activity and smoke optical  
861 depth in the Maritime Continent, *Atmos. Chem. Phys.*, 12(4), 2117–2147, doi:10.5194/acp-12-2117-2012, 2012.
- 862 Reid, J., Hyer, E., Johnson, R., Holben, B. N., Yokelson, R., Zhang, J., Campbell, J., Christopher, S., DiGirolamo, L., Giglio,  
863 L., Holz, R., Kearney, C., Miettinen, J., Reid, E., Turk, F. J., Wang, J., Xian, P., Zhao, G., Balasubramanian, R., Chew,

864 B. N., Janjai, S., Lagrosas, N., Lestari, P., Lin, N.-H., Mahmud, M., Nguyen, A. X., Norris, B., Oanth, N. T. K., Oo, M.,  
865 Salinas, S. V., Welton, E. J. and Liew, S. C.: Observing and understanding the Southeast Asian aerosol system by remote  
866 sensing: An initial review and analysis for the Seven Southeast Asian Studies (7SEAS) program, *Atmos. Res.*, 122, 403–  
867 468, doi:10.1016/j.atmosres.2012.06.005, 2013.

868 Reid, J. S., Lagrosas, N. D., Jonsson, H. H., Reid, E. A., Sessions, W. R., Simpas, J. B., Uy, S. N., Boyd, T. J., Atwood, S.  
869 A., Blake, D. R., Campbell, J. R., Cliff, S. S., Holben, B. N., Holz, R. E., Hyer, E. J., Lynch, P., Meinardi, S., Posselt, D.  
870 J., Richardson, K. A., Salinas, S. V., Smirnov, A., Wang, Q., Yu, L. and Zhang, J.: Observations of the temporal  
871 variability in aerosol properties and their relationships to meteorology in the summer monsoonal South China Sea/East  
872 Sea: the scale-dependent role of monsoonal flows, the Madden–Julian Oscillation, tropical cyclones, squall lines and cold  
873 pools, *Atmos. Chem. Phys.*, 15(4), 1745–1768, doi:10.5194/acp-15-1745-2015, 2015.

874 Reid, J. S., Xian, P., Holben, B. N., Hyer, E. J., Reid, E. A., Salinas, S. V., Zhang, J., Campbell, J. R., Chew, B. N., Holz, R.  
875 E., Kuciauskas, A. P., Lagrosas, N., Posselt, D. J., Sampson, C. R., Walker, A. L., Welton, E. J. and Zhang, C.: Aerosol  
876 meteorology of the Maritime Continent for the 2012 7SEAS southwest monsoon intensive study – Part 1: regional-scale  
877 phenomena, *Atmos. Chem. Phys.*, 16(22), 14041–14056, doi:10.5194/acp-16-14041-2016, 2016.

878 Ross, A. D., Holz, R. E., Quinn, G., Reid, J. S., Xian, P., Turk, F. J. and Posselt, D. J.: Exploring the First Aerosol Indirect  
879 Effect over the Maritime Continent Using a Ten-Year Collocated MODIS, CALIOP, and Model Dataset, *Atmos. Chem.*  
880 *Phys. Discuss.*, (March), 1–28, doi:10.5194/acp-2018-4, 2018.

881 Rolph, G., Stein, A., and Stunder, B. Real-time Environmental Applications and Display sYstem: READY. *Environmental*  
882 *Modelling & Software*, 95, 210-228, <https://doi.org/10.1016/j.envsoft.2017.06>. 2017.

883 Santoso, M., Lestiani, D. D., Mukhtar, R., Hamonangan, E., Syafrul, H., Markwitz, A. and Hopke, P. K.: Preliminary study  
884 of the sources of ambient air pollution in Serpong, Indonesia, *Atmos. Pollut. Res.*, 2(2), 190–196,  
885 doi:10.5094/apr.2011.024, 2011.

886 Schlosser, J. S., Braun, R. A., Bradley, T., Dadashazar, H., MacDonald, A. B., Aldhaif, A. A., Aghdam, M. A., Mardi, A. H.,  
887 Xian, P. and Sorooshian, A.: Analysis of aerosol composition data for western United States wildfires between 2005 and  
888 2015: Dust emissions, chloride depletion, and most enhanced aerosol constituents, *J. Geophys. Res. Atmos.*, 122(16),  
889 8951–8966, doi:10.1002/2017JD026547, 2017.

890 Seneviratne, M. C. S., Waduge, V. A., Hadagiripathira, L., Sanjeevani, S., Attanayake, T., Jayaratne, N. and Hopke, P. K.:  
891 Characterization and source apportionment of particulate pollution in Colombo, Sri Lanka, *Atmos. Pollut. Res.*, 2(2),  
892 207–212, doi:10.5094/apr.2011.026, 2011.

893 Shi, Y., Zhang, J., Reid, J. S., Liu, B., and Hyer, E. J.: Critical evaluation of cloud contamination in the MISR aerosol  
894 products using MODIS cloud mask products, *Atmos. Meas. Tech.*, 7, 1791-1801, 2014.

895 Song, Y., Xie, S., Zhang, Y., Zeng, L., Salmon, L. G. and Zheng, M.: Source apportionment of PM<sub>2.5</sub> in Beijing using  
896 principal component analysis/absolute principal component scores and UNMIX, *Sci. Total Environ.*, 372(1), 278–286,  
897 doi:10.1016/j.scitotenv.2006.08.041, 2006.

898 Sorooshian, A., Feingold, G., Lebsock, M. D., Jiang, H., and Stephens, G. L.: On the precipitation susceptibility of clouds to  
899 aerosol perturbations, *Geophys. Res. Lett.*, 36, L13803, doi:10.1029/2009GL038993, 2009.

900 Sowlat, M. H., Hasheminassab, S. and Sioutas, C.: Source apportionment of ambient particle number concentrations in  
901 central Los Angeles using positive matrix factorization (PMF), *Atmos. Chem. Phys.*, 16(8), 4849–4866, doi:10.5194/acp-  
902 16-4849-2016, 2016.

903 Stein, A.F., Draxler, R.R., Rolph, G.D., Stunder, B.J.B., Cohen, M.D., and Ngan, F. NOAA's HYSPLIT atmospheric  
904 transport and dispersion modeling system, *Bull. Amer. Meteor. Soc.*, 96, 2059-2077, [http://dx.doi.org/10.1175/BAMS-D-](http://dx.doi.org/10.1175/BAMS-D-14-00110.1)  
905 [14-00110.1](http://dx.doi.org/10.1175/BAMS-D-14-00110.1), 2015.

906 Thurston, G. D., Ito, K. and Lall, R.: A Source Apportionment of U.S. Fine Particulate Matter Air Pollution, *Atmos.*  
907 *Environ.*, 45(24), 3831–3840, doi: 10.1016/j.atmosenv.2011.04.070, 1994.

908 Tian, S. L., Pan, Y. P. and Wang, Y. S.: Size-resolved source apportionment of particulate matter in urban Beijing during  
909 haze and non-haze episodes, *Atmos. Chem. Phys.*, 16(1), 1–19, doi:10.5194/acp-16-1-2016, 2016.

910 Twohy, C. H., Kreidenweis, S. M., Eidhammer, T., Browell, E. V., Heymsfield, A. J., Bansemer, A. R., Anderson, B. E.,  
911 Chen, G., Ismail, S., DeMott, P. J. and Van Den Heever, S. C.: Saharan dust particles nucleate droplets in eastern  
912 Atlantic clouds, *Geophys. Res. Lett.*, 36(1), L01807, doi:10.1029/2008GL035846, 2009.

913 Van Pinxteren, D., Fomba, K. W., Spindler, G., Müller, K., Poulain, L., Iinuma, Y., Löschau, G., Hausmann, A. and  
914 Herrmann, H.: Regional air quality in Leipzig, Germany: Detailed source apportionment of size-resolved aerosol  
915 particles and comparison with the year 2000, *Faraday Discuss.*, 189, 291–315, doi:10.1039/c5fd00228a, 2016.

916 Venecek, M. A., Zhao, Y., Mojica, J., McDade, C. E., Green, P. G., Kleeman, M. J. and Wexler, A. S.: Characterization of  
917 the 8-stage Rotating Drum Impactor under low concentration conditions, *Journal of Aerosol Science*, 100, 140–154,  
918 doi:10.1016/j.jaerosci.2016.07.007, 2016.

919 Viana, M., Kuhlbusch, T. A. J., Querol, X., Alastuey, A., Harrison, R. M., Hopke, P. K., Winiwarter, W., Vallius, M., Szidat,  
920 S., Prévôt, A. S. H., Hueglin, C., Bloemen, H., Wählin, P., Vecchi, R., Miranda, A. I., Kasper-Giebl, A., Maenhaut, W.

921 and Hitzenberger, R.: Source apportionment of particulate matter in Europe: A review of methods and results, *J. Aerosol*  
922 *Sci.*, 39(10), 827–849, doi:10.1016/j.jaerosci.2008.05.007, 2008.

923 Visser, S., Slowik, J. G., Furger, M., Zotter, P., Bukowiecki, N., Canonaco, F., Flechsig, U., Appel, K., Green, D. C.,  
924 Tremper, A. H., Young, D. E., Williams, P. I., Allan, J. D., Coe, H., Williams, L. R., Mohr, C., Xu, L., Ng, N. L.,  
925 Nemitz, E., Barlow, J. F., Haliou, C. H., Fleming, Z. L., Baltensperger, U. and Prévôt, A. S. H.: Advanced source  
926 apportionment of size-resolved trace elements at multiple sites in London during winter, *Atmos. Chem. Phys.*, 15(19),  
927 11291–11309, doi:10.5194/acp-15-11291-2015, 2015.

928 Wang, B., Wu, R. and Fu, X.: Pacific–East Asian Teleconnection: How Does ENSO Affect East Asian Climate?, *J. Clim.*,  
929 13(9), 1517–1536, doi:10.1175/1520-0442(2000)013<1517:PEATHD>2.0.CO;2, 2000.

930 Wang, S.-H., Tsay, S.-C., Lin, N.-H., Hsu, N. C., Bell, S. W., Li, C., Ji, Q., Jeong, M.-J., Hansell, R. A., Welton, E. J.,  
931 Holben, B. N., Sheu, G.-R., Chu, Y.-C., Chang, S.-C., Liu, J.-J. and Chiang, W.-L.: First detailed observations of long-  
932 range transported dust over the northern South China Sea, *Atmos. Environ.*, 45(27), 4804–4808,  
933 doi:10.1016/j.atmosenv.2011.04.077, 2011.

934 Wang, Z., Sorooshian, A., Prabhakar, G., Coggon, M. M. and Jonsson, H. H.: Impact of emissions from shipping, land, and  
935 the ocean on stratocumulus cloud water elemental composition during the 2011 E-PEACE field campaign, *Atmos.*  
936 *Environ.*, 89, 570–580, doi:10.1016/j.atmosenv.2014.01.020, 2014.

937 Webster, P. J., Magana, V. O., Palmer, T. N., Shukla, J., Tomas, R. A., Yanai, M. and Yasunari, T.: Monsoons : Processes ,  
938 predictability , and the prospects for prediction 2 . Description of the Monsoons, *Weather*, 103(C7), 14451–14510, 1998.

939 Weichenthal, S., Villeneuve, P. J., Burnett, R. T., Donkelaar, A. van, Martin, R. V., Jones, R. R., DellaValle, C. T., Sandler,  
940 D. P., Ward, M. H. and Hoppin, J. A.: Long-Term Exposure to Fine Particulate Matter: Association with Nonaccidental  
941 and Cardiovascular Mortality in the Agricultural Health Study Cohort, *Environ. Health Perspect.*, 122(6), 609–615,  
942 doi:10.1289/ehp.1307277, 2014.

943 Wimolwattanapun, W., Hopke, P. K. and Pongkiatkul, P.: Source apportionment and potential source locations of PM<sub>2.5</sub> and  
944 PM<sub>2.5–10</sub> at residential sites in metropolitan Bangkok, *Atmos. Pollut. Res.*, 2(2), 172–181, doi:10.5094/apr.2011.022,  
945 2011.

946 Witt, M., Baker, A. R. and Jickells, T. D.: Atmospheric trace metals over the Atlantic and South Indian Oceans:  
947 Investigation of metal concentrations and lead isotope ratios in coastal and remote marine aerosols, *Atmos. Environ.*,  
948 40(28), 5435–5451, doi:10.1016/j.atmosenv.2006.04.041, 2006.

949 Wu, C., Larson, T. V., Wu, S., Williamson, J., Westberg, H. H. and Liu, L.-J. S.: Source apportionment of PM<sub>2.5</sub> and  
950 selected hazardous air pollutants in Seattle, *Sci. Total Environ.*, 386(1–3), 42–52, doi:10.1016/j.scitotenv.2007.07.042,  
951 2007.

952 Xian, P., Reid, J. S., Atwood, S. A., Johnson, R. S., Hyer, E. J., Westphal, D. L. and Sessions, W.: Smoke aerosol transport  
953 patterns over the Maritime Continent, *Atmos. Res.*, 122, 469–485, doi:10.1016/j.atmosres.2012.05.006, 2013.

954 Xie, R. K., Seip, H. M., Liu, L. and Zhang, D. S.: Characterization of individual airborne particles in Taiyuan City, China,  
955 *Air Qual. Atmos. Heal.*, 2(3), 123–131, doi:10.1007/s11869-009-0039-x, 2009.

956 Xing, Y. F., Xu, Y. H., Shi, M. H. and Lian, Y. X.: The impact of PM<sub>2.5</sub> on the human respiratory system, *J. Thorac. Dis.*,  
957 8(1), E69–E74, doi:10.3978/j.issn.2072-1439.2016.01.19, 2016.

958 Yuan, B., Shao, M., Gouw, J. de, Parrish, D. D., Lu, S., Wang, M., Zeng, L., Zhang, Q., Song, Y., Zhang, J. and Hu, M.:  
959 Volatile organic compounds (VOCs) in urban air: How chemistry affects the interpretation of positive matrix  
960 factorization (PMF) analysis, *J. Geophys. Res. Atmos.*, 117(D24), 1-17, doi:10.1029/2012jd018236, 2012.

961 Yusuf, A. A. and Francisco, H.: Climate change vulnerability mapping for Southeast Asia, *Economy and Environment*  
962 *Program for Southeast Asia (EEPSEA) report*, available at: <http://www.eepsea.net> (last access: July 2014), 32 pp., 2009.

963 Zhang, C.: Madden-Julian Oscillation, *Rev. Geophys.*, 43, RG2003, doi:10.1029/2004RG000158, 2005.

964 Zhang, J. and Reid, J. S.: MODIS Aerosol Product Analysis for Data Assimilation: Assessment of Level 2 Aerosol Optical  
965 Thickness Retrievals, *J. Geophys. Res.-Atmos.*, 111, 22207, doi:10.1029/2005JD006898, 2006.

966 Zheng, C., Zhao, C., Zhu, Y., Wang, Y., Shi, X., Wu, X., Chen, T., Wu, F. and Qiu, Y.: Analysis of influential factors for the  
967 relationship between PM<sub>2.5</sub> and AOD in Beijing, *Atmos. Chem. Phys.*, 17(21), 13473–13489, doi:10.5194/acp-17-  
968 13473-2017, 2017.

969 Zivanovic, V.: XRF analysis of mineralogical matrix effects and differences between pulverized and fused ferromanganese  
970 slag, *Chem. Ind. Chem. Eng. Q.*, 17(2), 231–237, doi:10.2298/ciceq101104008z, 2011.

971 **Table 1. PM1.15/PM10 ratio slopes for elements ordered by ratio-slope.**

	<i>Ratio slope</i>	<i>R-squared correlation</i>	<i>Ratio average</i>	<i>Standard deviation</i>
<b>V</b>	0.94	0.99	0.95	0.07
<b>K</b>	0.82	0.94	0.35	0.21
<b>S</b>	0.8	0.92	0.49	0.17
<b>Zn</b>	0.74	0.94	0.62	0.04
<b>Y</b>	0.7	0.7	0.53	0.11
<b>Zr</b>	0.7	0.63	0.65	0.07
<b>Mo</b>	0.7	0.67	0.65	0.04
<b>Ti</b>	0.68	0.7	0.53	0.08
<b>Rb</b>	0.61	0.64	0.73	0.09
<b>Al</b>	0.51	0.68	0.55	0.12
<b>Pb</b>	0.47	0.44	0.67	0.06
<b>Cu</b>	0.4	0.42	0.63	0.05
<b>Ni</b>	0.31	0.33	0.61	0.08
<b>As</b>	0.31	0.36	0.33	0.26
<b>Mn</b>	0.3	0.62	0.49	0.19
<b>Si</b>	0.29	0.56	0.32	0.13
<b>Se</b>	0.2	0.24	0.59	0.06
<b>P</b>	0.19	0.32	0.27	0.08
<b>Na</b>	0.16	0.57	0.17	0.03
<b>Sr</b>	0.16	0.11	0.49	0.08
<b>Br</b>	0.13	0.17	0.47	0.08
<b>Ca</b>	0.07	0.59	0.1	0.05
<b>Cl</b>	0.06	0.67	0.04	0.02
<b>Fe</b>	0.06	0.38	0.24	0.12
<b>Mg</b>	0.03	0.29	0.07	0.03
<b>Co</b>	0.03	0.03	0.57	0.1
<b>Ga</b>	0.03	0.04	0.56	0.09
<b>Cr</b>	0.01	0.02	0.19	0.19

972



973 **Table 2. Sources identified in each size range with PMF. Coarse (1.15-10  $\mu\text{m}$ ), fine (0.34-1.15  $\mu\text{m}$ ) and ultrafine (0.10-**  
 974 **0.34  $\mu\text{m}$ ).**

Source	Major Components	Coarse	Fine	Ultrafine
<b>Biomass Burning</b>	K, S, Si, Al, As		+	+
<b>Oil Combustion</b>	V		+	+
<b>Crustal-Marine Mixed Source</b>	Mg, Cl, P, Al, Si, S, Ca	+		
<b>Sea Spray</b>	Na, Mg, Cl, Ca		+	
<b>Soil Dust</b>	Fe, Al, Si, Ca, Ti, Zn	+	+	
<b>Fly ash</b>	As, Se, Pb, Zn, Ti	+	+	+

975

976